

# Deposition and Analysis of Zinc Oxide Thin Films by Pulsed Laser Deposition

DIPLOMARBEIT

Friedrich-Schiller-Universität Jena  
Physikalisch-Astronomische Fakultät  
Institut für Festkörperphysik

eingereicht von: Robert Pietzcker  
geboren am: 26.05.1981 in: Bonn

1. Gutachter:

Prof. Dr. Paul Seidel

2. Gutachter:

PD Dr. Frank Schmidl

Tag der Verleihung des Diploms:

# Erklärung

Ich erkläre, dass ich die vorliegende Arbeit selbständig verfasst und keine anderen als die angegebenen Quellen und Hilfsmittel benutzt habe.

Jena, den

Unterschrift

Seitens des Verfassers bestehen keine Einwände, die vorliegende Diplomarbeit für die öffentliche Nutzung in der Thüringer Universitäts- und Landesbibliothek zur Verfügung zu stellen.

Jena, den

Unterschrift



# Acknowledgments

I would like to express my gratitude to all those who assisted me academically and personally in finishing this part of my studies and completing this thesis.

My special thanks go to Prof. Dr. P. Seidel for the possibility to write my thesis in his low temperature research group and for accepting the responsibility to supervise my work.

I am deeply indebted to my direct supervisor, PD F. Schmidl, who inspired me to conduct research on thin films. He was always open for discussion, conveyed motivation and energy, and left me all the liberties for self-determined work.

My thanks go to Mr. Hanse, who designed and fabricated all parts needed for the changes to the PLD setup, and Lutz Föllmer and Torsten Hilbrecht, who tirelessly helped when problems with the PLD setup occurred.

To Dr. Kräußlich for his advice on XRD measurements.

To Ms. Voigt for the Dektak and AFM measurements.

To Veit Grosse, for his guidance and advice in all things PLD- and YBCO-related.

To Micha Mans, for his unlimited willingness to help and his patience to endure my questions and music.

To Gabriel Zieger, who assisted me in unraveling the mysteries of PLD and scientific work, and who was there whenever I needed help to rebuild the setup or discuss physics, environmental science or politics.

To the whole research group for the great atmosphere and the absolute willingness to help each other.

To my parents, whose support (both moral and monetary) enabled me to study physics and write this thesis.

To Michala Garbe, without whom this thesis would never have been created.

To my roommates, who were a source of joy and laughter and always there when I needed a diversion from physics.

To Vroni Bierbaum, for her friendship, support, and witty comments throughout the last six years.

To Jette Gruber, for long hours of Tango Argentino and her encouragement to change the world.

To Ara Schorscher-Petcu, for her friendship, her inspiration to own thoughts and perceptions, and her influence on my life from afar.

# Contents

<b>Acknowledgments</b>	<b>V</b>
<b>Introduction</b>	<b>1</b>
<b>1 Fundamentals</b>	<b>3</b>
1.1 Crystallography . . . . .	3
1.1.1 Lattice spacing calculation . . . . .	3
1.1.2 Polycrystalline materials . . . . .	3
1.2 Thin film growth . . . . .	4
1.2.1 Pulsed laser deposition (PLD) . . . . .	5
1.2.2 Layer growth . . . . .	9
1.3 Superconductivity . . . . .	11
1.4 $\text{YBa}_2\text{Cu}_3\text{O}_{7-x}$ . . . . .	12
1.4.1 Crystal structure . . . . .	12
1.4.2 Growth mechanisms of YBCO thin films . . . . .	12
1.5 Zinc oxide (ZnO) . . . . .	14
1.5.1 Crystal structure . . . . .	14
1.5.2 Electric properties . . . . .	15
1.5.3 Pulsed laser deposition of ZnO . . . . .	15
<b>2 Experimental setup: sample preparation</b>	<b>17</b>
2.1 Pulsed laser deposition (PLD) setup . . . . .	17
2.2 Deposition process . . . . .	18
2.3 Patterning of the YBCO films . . . . .	19
<b>3 Analytical methods</b>	<b>20</b>
3.1 Profilometry . . . . .	20
3.2 Rutherford backscattering spectroscopy (RBS) . . . . .	20
3.3 Atomic force microscopy (AFM) . . . . .	21
3.4 Scanning electron microscopy (SEM) . . . . .	22
3.5 $R(T)$ -measurements . . . . .	22
3.6 $j_C$ -measurements . . . . .	24
3.7 X-ray diffraction (XRD) . . . . .	24
3.7.1 X-ray diffractometer . . . . .	24
3.7.2 Lattice spacing and crystallite size . . . . .	24
3.7.3 Crystal orientation . . . . .	27
3.7.4 Evaluation of the XRD data . . . . .	27

3.7.5	Accuracy of the measurements . . . . .	28
<b>4</b>	<b>Experimental results and discussion</b>	<b>30</b>
4.1	Changes to the pulsed laser deposition system . . . . .	30
4.1.1	Target treatment . . . . .	30
4.1.2	Laser focus . . . . .	31
4.1.3	Droplet density . . . . .	33
4.1.4	Heater . . . . .	34
4.2	Optimization of the YBCO layer . . . . .	36
4.2.1	Layer thickness of YBCO films . . . . .	36
4.2.2	Surface of YBCO films . . . . .	36
4.2.3	Crystallinity of YBCO films . . . . .	39
4.2.4	Superconducting properties of YBCO films . . . . .	44
4.2.5	Relation between c-axis length and superconducting properties . .	46
4.3	Analysis of the ZnO layer . . . . .	48
4.3.1	General remarks . . . . .	48
4.3.2	Surface of the ZnO layer . . . . .	49
4.3.3	Crystallinity of the ZnO layer . . . . .	52
4.3.4	YBCO degradation due to ZnO deposition . . . . .	57
4.3.5	Optimal deposition conditions . . . . .	58
4.3.6	Comparison of different substrates . . . . .	58
<b>5</b>	<b>Conclusion and outlook</b>	<b>59</b>

# List of Figures

1.1	Out-of-plane and in-plane orientation. . . . .	4
1.2	Sketch of the PLD setup in on-axis geometry. . . . .	5
1.3	YBCO film with many droplets (SEM picture, SE mode). . . . .	6
1.4	Cones on YBCO target after PLD (OM pictures). . . . .	7
1.5	Substrate position for a) on-axis PLD b) off-axis PLD. . . . .	8
1.6	Two-beam PLD setup allowing particle-free film deposition [1]. . . . .	9
1.7	The three main thin film growth modes. . . . .	10
1.8	Critical surface phase diagram for Type I superconductivity. . . . .	11
1.9	YBCO phases and phase diagram. . . . .	13
1.10	ZnO in the hexagonal wurtzite structure [2], [3]. . . . .	14
1.11	Sketch of the PLD setup in on-axis geometry. . . . .	16
2.1	Laser scan pattern on target. . . . .	17
2.2	Ion-etched $j_C$ -bridge (SEM picture, SE mode). . . . .	19
3.1	Sample RBS spectrum. . . . .	21
3.2	Sample $R(T)$ -measurement of an YBCO film. . . . .	23
3.3	Sketch of Bragg-Brentano X-ray diffractometer. . . . .	25
3.4	The angles accessible by the four-circle goniometer. . . . .	25
3.5	XRD chart: $STO_{002}$ peak. . . . .	26
3.6	XRD chart: rocking curves. . . . .	28
4.1	YBCO and ZnO target surface. . . . .	31
4.2	Laser focus at target site. . . . .	32
4.3	YBCO target after deposition. . . . .	32
4.4	OM pictures to compare droplet densities. . . . .	33
4.5	SEM pictures to compare droplet densities. . . . .	34
4.6	Clamping heater before and after deposition. . . . .	35
4.7	YBCO films: rough surface of sample 322. . . . .	37
4.8	YBCO films: precipitates on sample 372. . . . .	38
4.9	YBCO films: precipitates on sample 369. . . . .	38
4.10	YBCO films: smooth surface on sample 366. . . . .	39
4.11	YBCO films: surface roughness vs. temperature. . . . .	40
4.12	YBCO films: surface roughness vs. laser fluence. . . . .	40
4.13	YBCO films: $2\Theta$ vs. temperature. . . . .	42
4.14	YBCO films: rocking curve vs. pressure. . . . .	43
4.15	Photos of plasma plume from YBCO target. . . . .	43



4.16	YBCO films: rocking curve vs. temperature. . . . .	44
4.17	YBCO films: critical temperature vs. substrate temperature. . . . .	45
4.18	YBCO films: superconducting transition width vs. substrate temperature. . . . .	46
4.19	YBCO films: critical temperature vs. c-axis length. . . . .	47
4.20	YBCO films: critical temperature vs. calculated oxygen content. . . . .	47
4.21	Photos of plasma plume from ZnO. . . . .	48
4.22	ZnO films: smooth surface of sample 362. . . . .	49
4.23	ZnO films: surface of sample 380. . . . .	49
4.24	ZnO films: surface roughness vs. substrate temperature. . . . .	50
4.25	ZnO films: AFM pictures of chosen sample. . . . .	51
4.26	XRD chart: $\omega$ - $2\theta$ -scan of sample with ZnO on YBCO on STO. . . . .	52
4.27	ZnO films: $2\theta$ of ZnO <sub>001</sub> vs. substrate temperature. . . . .	53
4.28	ZnO films: crystallite size vs. substrate temperature. . . . .	54
4.29	ZnO films: Rocking curve vs. substrate temperature. . . . .	55
4.30	ZnO films: $\phi$ -scan of sample 385. . . . .	56
4.31	ZnO films: $\phi$ -scan vs rocking curve. . . . .	56
4.32	Lattice positioning of ZnO on YBCO. . . . .	57
4.33	ZnO films: YBCO $2\theta$ vs. substrate temperature. . . . .	58

# Glossary

$\Delta T_C$ :  $T_C(10\%) - T_C(90\%)$ , 23

$\Delta_\omega$ : FWHM of rocking curve, 27

$\Delta_{2\theta}$ : FWHM of  $\omega$ - $2\theta$ -scan, 24

AFM: atomic force microscopy, 21

FWHM: full width at half maximum, 26

OM: optical microscope, 33

PLD: pulsed laser deposition, 4

rms: root mean square, 22

SAW: surface acoustic wave guides, 14

SEM BSE: scanning electron microscopy using backscattered electrons, 22

SEM SE: scanning electron microscopy using secondary electrons, 22

SEM: scanning electron microscopy, 22

STO : strontium titanate,  $\text{SrTiO}_3$ , 13

$T_C(10\%)$ : temperature at which the resistance dropped by 10% of the linear fit of the normal resistance, 23

$T_C(90\%)$ : temperature at which the resistance dropped by 90% of the linear fit of the normal resistance, 23

TCO: transparent conducting oxides, 14

YBCO : Yttrium Barium Copper Oxide,  $\text{YBa}_2\text{Cu}_3\text{O}_{7-x}$ , 1

ZnO: Zinc Oxide, 1

# Introduction

The fabrication of superconducting microelectronic devices has received much attention over the last two decades, but there remains a lot to do. One field of interest is the analysis of dielectric films needed as isolating layers for multilayer device fabrication. This research group has accumulated knowledge about the deposition and analysis of  $\text{YBa}_2\text{C}_3\text{O}_{7-x}$  (YBCO) superconducting films on different substrates and subsequent deposition of dielectric films like  $\text{CeO}_x$ ,  $\text{SiO}_2$  or  $\text{SrTiO}_3$  (STO).

Zinc oxide (ZnO) is a wide-bandgap semiconductor which has been studied for 60 years, but received renewed attention in very different fields over the last ten years, one of which are the applications of ZnO films: the resistivity of ZnO films is tunable through doping over a wide range ( $10^{-4}$ - $10^9 \Omega \text{ cm}$ ), making it promising for both low-resistivity applications like transparent conducting oxides (TCO) and - together with its piezoelectric effect - high-resistivity applications like surface acoustic wave guides (SAW).

While there exist several theoretical approaches that attempt to describe the different stages of thin film growth, it remains an empirical field of studies in many areas with emphasis on a descriptive approach. The number of arriving and interacting particles is so large that exact microscopic modeling is beyond the calculation capacity of modern computers. Meanwhile, the time scales of the adsorption/ordering/surface diffusion processes are so short that the process is far from thermal equilibrium, making macroscopic thermodynamic models soon reach the limits of their usefulness. This is also an experimental problem: the experimenter is only able to influence the thermodynamic parameters like average deposition pressure or average substrate temperature. However, the growth process in itself is so sensitive to minor local variations that even perfect control of the average thermodynamic parameters (which of course cannot be reached due to shortcomings of material and measuring equipment) would not result in exactly reproducible films. Therefore a qualitative descriptive approach looking for general trends is best combined with a high tolerance for outliers.

To contribute to the investigations into ZnO films and the possibility of using them as isolating layers in superconducting microelectronic devices, the growth of smooth epitaxial ZnO thin films on YBCO layers grown on STO substrates is studied in this thesis.

Knowledge about the ohmic or Schottky qualities of the interface between the ZnO film, the YBCO film and a possible top electrode layer is important for future applications. To acquire this knowledge through electrical measurements, films with reproducible interfaces must be deposited. As precipitates, droplets and other surface defects will influence this interface in a non-predictable way, smooth interfaces both between

YBCO and ZnO and between ZnO and a top electrode are essential.

The crystallinity and degree of ordering has a strong impact on the electrical properties of the YBCO films as well as on the electrical and optical properties of the ZnO films. For YBCO, the long range order influences both the critical temperature and the critical current density, while for ZnO, defect sites at grain boundaries change both charge carrier density and conducting mechanisms. Furthermore, the additional energy levels will influence the photoluminescence spectrum. Therefore, special emphasis is placed on the reproducible fabrication of highly epitaxial films with good out-of-plane orientation.

The combination of a superconductor and a direct semiconductor creates a range of interesting physical phenomena to be studied, e.g., the influence of changing the charge carrier density in ZnO through illumination with UV light on the superconducting behavior of the underlying YBCO layer. Depositing high-resistivity ZnO on YBCO allows the analysis of an isolating barrier with piezoelectric properties on a superconductor.

In chapter 1, an introduction into the main topics of this thesis is given. A short discussion of crystallography presents the calculation of lattice spacings and lattice angles in orthorhombic and hexagonal crystal systems. Later on, the fundamentals of film growth as well as the advantages and disadvantages of pulsed laser deposition will be discussed. Finally, the two materials studied in this thesis, YBCO and ZnO, are introduced. Material properties as well as a short overview over previous work are presented.

In chapter 2, the experimental setup is described. A presentation of the sample preparation and deposition process is followed by a short paragraph about the patterning of the films.

Chapter 3 is dedicated to a discussion of the analytic tools used to characterize the films. Special emphasis is placed on the discussion of X-ray analysis.

In chapter 4, the experimental results are presented and discussed. A detailed analysis of the optimization of the YBCO layers towards smoothness and high crystallinity is followed by a discussion of the influence of oxygen pressure, substrate temperature and deposition time on surface and morphology of the ZnO films deposited on YBCO.

Finally, chapter 5 will offer a summary of results as well as an outlook on future research necessary in this area.

# 1 Fundamentals

## 1.1 Crystallography

A perfect crystal structure can be described as the combination of one of the 14 Bravais lattices with a basis of atoms or molecules positioned inside each unit cell of the Bravais lattice.

### 1.1.1 Lattice spacing calculation

To calculate the plane spacing  $d_{hkl}$  for crystal planes indexed with Miller indices (hkl) in a crystal with lattice parameters a, b, c, the following two formulas were used [4]:

$d_{hkl}$  for orthorhombic crystals, e.g., YBCO:

$$\frac{1}{d_{hkl}^2} = \frac{h^2}{a^2} + \frac{k^2}{b^2} + \frac{l^2}{c^2}, \quad (1.1)$$

$d_{hkl}$  for hexagonal crystals, e.g., ZnO:

$$\frac{1}{d_{hkl}^2} = \frac{4}{3} \left( \frac{h^2 + hk + k^2}{a^2} \right) + \frac{l^2}{c^2}. \quad (1.2)$$

The angle  $\alpha_{hkl}$  between a crystal plane (hkl) and the c-axis (necessary for the determination of in-plane-orientation as well as the evaluation of a-axis growth in YBCO) was calculated according to [4]:

$\alpha_{hkl}$  for orthorhombic crystals, e.g., YBCO:

$$\cos(\alpha_{hkl}) = \frac{l/c}{\sqrt{(h^2/a^2) + (k^2/b^2) + (l^2/c^2)}}, \quad (1.3)$$

$\alpha_{hkl}$  for hexagonal crystals, e.g., ZnO:

$$\cos(\alpha_{hkl}) = \sqrt{\frac{(3a^2/4c^2)l^2}{h^2 + k^2 + hk + (3a^2/4c^2)l^2}}. \quad (1.4)$$

### 1.1.2 Polycrystalline materials

While perfect single crystals are ordered in all directions, most materials exist in different states of ordering: when there is no long-range order, a material is called amorphous.

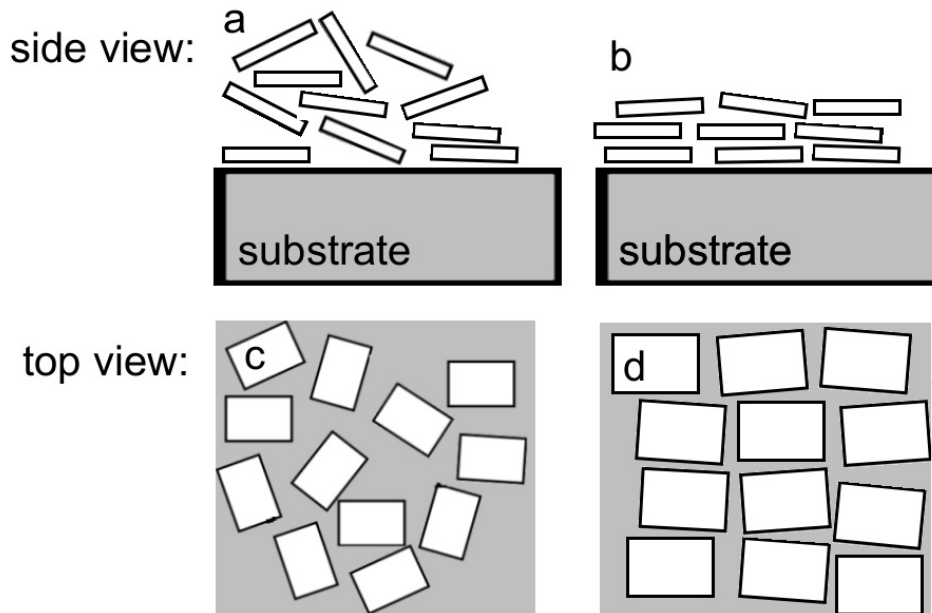


Figure 1.1: Different degrees of ordering: a) low out-of-plane orientation b) high out-of-plane orientation c) low in-plane orientation d) high in-plane orientation.

Polycrystalline material consists of grains which are well-ordered in themselves but have little long-range order beyond the boundaries of one grain.

When analyzing polycrystalline films, one differentiates between out-of-plane and in-plane orientation (see fig. 1.1). A film has a high out-of-plane orientation when the  $c$ -axis is parallel to the surface normal. In-plane-orientation goes a step further: it measures how well the  $a, b$ -axes of different crystallites are aligned to each other in the plane.

## 1.2 Thin film growth

For this thesis, I limit myself to the study of thin films grown by pulsed laser deposition (PLD)<sup>1</sup>. PLD is a simple and versatile technique that allows stoichiometric growth of a huge variety of composite materials. Some advantages are the simplicity of the process (the small targets required are relatively cheap and easy to fabricate), the precise control of film thickness, and the possibility to have a high background pressure of a chosen reactive gas (up to a few hundred Pascal).

However, PLD also has two main disadvantages: it is difficult to obtain uniform high-quality films on large substrates due to the narrow angular distribution of the plasma plume, and it is very difficult to prevent "splashing", i.e. the deposition of large particles or droplets on the newly-grown film.

<sup>1</sup>The following paragraphs heavily rely on the book "Pulsed Laser Deposition of thin films" [5] which presents a thorough treatment of the development of PLD up to 1993, discussing both the experimental details as well as the theoretical models used to describe film growth, even detailing some modifications of the setup for specific materials.

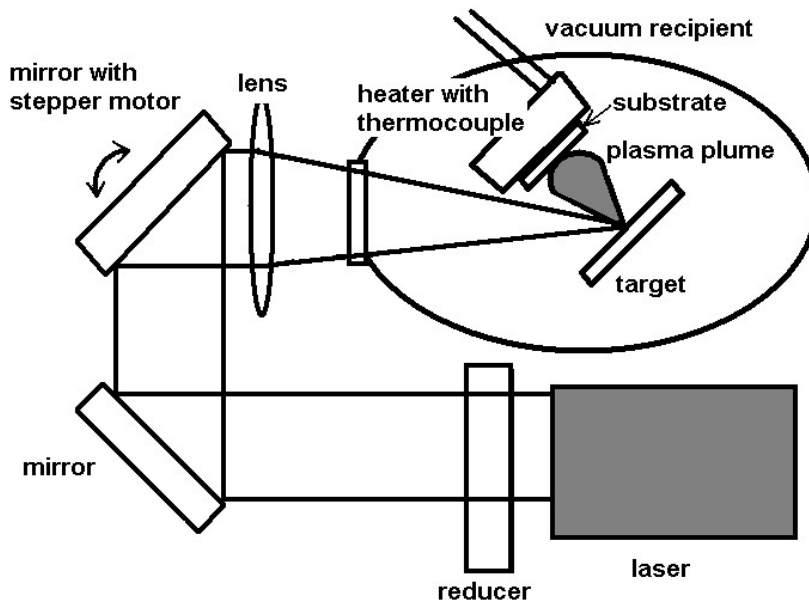


Figure 1.2: Sketch of the PLD setup in on-axis geometry.

For an overview of other methods of thin film growth, the textbook "Oberflächen- und Dünnschicht-Technologie" [6] is recommended, presenting both physical and chemical vapor deposition techniques and their applications.

### 1.2.1 Pulsed laser deposition (PLD)

In pulsed laser deposition, nanosecond laser pulses of high fluence ( $0.5-10 \text{ J cm}^{-2}$ ) are focused on a target. The high energy density leads to an explosive vaporization of the top 50-500 nm, producing a plasma plume of high energy particles (10-200 eV) perpendicular to the target surface. Due to the almost instantaneous vaporization, no thermal equilibrium is reached, therefore even composite materials made from elements with very different vapor pressures are uniformly ablated [7].

PLD allows independent control of process parameters like laser fluence, background gas pressure, background gas composition, substrate temperature and substrate position in respect to the plasma plume. As the initial velocity of the ablated particles is very high ( $5 - 35 \times 10^3 \text{ ms}^{-1}$  [8], [7]), PLD can be performed at gas pressures as high as 1 kPa.

The most commonly used setup of the PLD system is the on-axis geometry, meaning that the substrate is parallel to the target positioned in the middle of the plasma plume (see fig. 1.2). This setup leads to high deposition rates and a high uniformity of the deposited films. Furthermore, the incidence of particles perpendicular to the substrate surface can improve the alignment of c-axis growth through an angle-dependent re-sputtering/ablation effect, as Patzig reports [9].

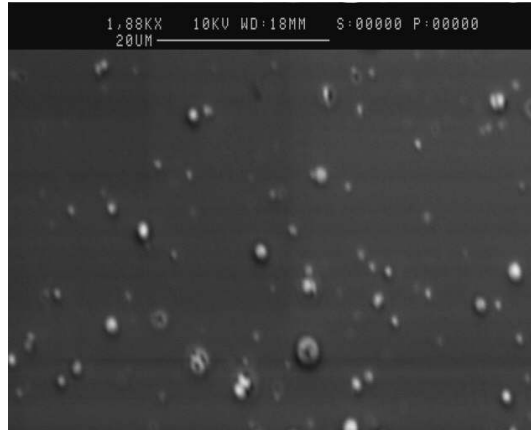


Figure 1.3: YBCO film with many droplets (SEM picture, SE mode).

### Ablation Process

The ablation process can be described with the sub-surface superheating model [10]: for materials like YBCO or ZnO, the energy of the incoming short-wavelength laser pulse is absorbed within the first 10-100 nm. The surface is quickly (4-6 ns) heated to temperatures around 2000 K, leading to sublimation of the topmost layer and accordingly, to cooling of the adjacent regions due to the extracted heat of vaporization. Lower layers continue to absorb the laser energy, reaching much higher temperatures, which finally leads to an explosive vaporization away from the target. The particles therefore have a high kinetic energy with a strong forward component which can be described through a shifted Maxwell-Boltzmann distribution on a stream velocity [11].

The ablated material forms a dense plasma layer ( $n > 10^{19} \text{ cm}^{-3}$ ) called Knudsen layer a few tens of nm above the target surface [7], [12]. In this plasma, the high energy particles thermalize, leading to plasma temperatures of about 10000 K. While the plasma expands, it continues to absorb laser energy through inverse Bremsstrahlung absorption, leading to an isothermal expansion. When the laser pulse ends, the plasma finally expands adiabatically, re-transforming thermal into kinetic energy [5].

The angular distribution of the particle flux (and therefore the resulting film thicknesses  $d$ ) depend on the angle  $\Theta$  between substrate and target normal through a  $\cos^n(\Theta)$  distribution. The exponent  $n$  depends on the energy density of the laser pulse, having values between 1 (insufficient energy density leading to thermal evaporation) and 12 [7]. Due to this strong angular dependence, PLD is mainly used for thin film deposition on small substrates ( $1 \times 1 \text{ cm}^2$ ). Larger substrates require rotating holders, a broadened laser plume through use of a focus line instead of a focus spot [13], or multiple laser plumes [14].

### Droplets

One major problem of PLD-grown films are droplets - clusters with diameters between 100 nm and a few microns which damage the newly-grown film and lead to very rough



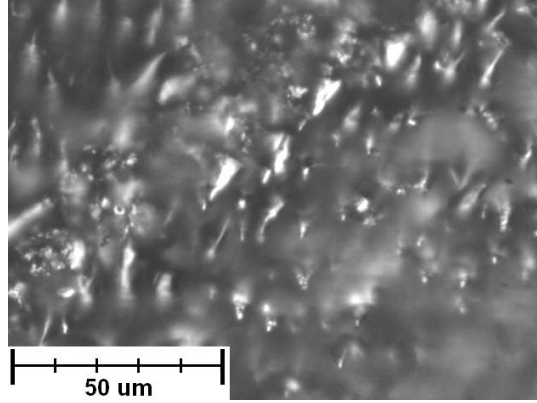


Figure 1.4: Cones on YBCO target after PLD (OM pictures).

film surfaces (see fig. 1.3).

As seen in previous works, the target surface deteriorates in the PLD process [15]. Each shot ablates some material, but there always are surrounding areas which are heated only to their melting point and not to the point of evaporation or even plasma-formation. The melted areas form cone-like structures (see fig. 1.4) of changed composition which change the absorption of the laser pulse and which may explode off the target during subsequent laser shots without being vaporized, leading to large droplets ( $0.5 - 2 \mu\text{m}$ ) on the substrate [5]. It is therefore necessary to sand the target before each deposition to reduce the number of droplets and keep the deposition rate constant [15].

Droplet formation increases when the laser energy is too high, too low or unevenly distributed: the subsurface layers explode before the upper layers have absorbed enough energy to be evenly vaporized in the process. The laser wavelength also has a large influence on droplet formation. In a comparison between infrared, visible and ultra-violet PLD, the UV lasers result in the lowest droplet densities [16].

Over the last 20 years, a variety of experimental methods, including off-axis deposition [17], [18], a mechanical high-speed shutter [19], target modification [12], oscillating scanning in which the target revolves while being scanned [20], use of a shadow mask [21], [22] and the use of two synchronized laser beams [1] have been used to decrease the droplet density on YBCO films from the usual  $10^6$ - $10^7 \text{ cm}^{-2}$  [23] down to  $10^2$ - $10^5 \text{ cm}^{-2}$ . However, all of these methods have their drawbacks or require extensive (and expensive) upgrading of the ordinary PLD setup:

In off-axis geometry, the substrate is held at an angle to the plasma plume particles, sometimes even turned backwards so that only particles scattered to the side or back of the plume reach the substrate surface (see fig. 1.5). This reduces the deposition rate and often leads to non-uniform films as the edge closer to the target grows much faster than the one further away; also the stoichiometry can change [24], [25]. In addition, it reduces droplet density. The droplets are much heavier than the atoms and ions in a plasma plume, so they get scarcely scattered sideways out of the plume. The non-uniformity can be overcome by using a rotating substrate holder [18], [26]. Also, the off-axis geometry with an angle of  $\sim 40^\circ$  between target and substrate was shown to be of advantage for

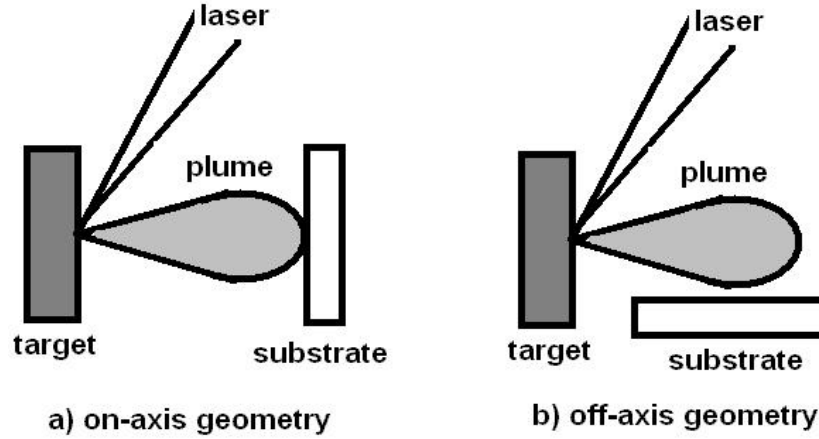


Figure 1.5: Substrate position for a) on-axis PLD b) off-axis PLD.

the even deposition of YBCO on substrates with step edges to be used for Josephson junctions [27].

The target composition is of importance: adding 30 wt. % Ag to the YBCO target before sintering decreased the droplet density down to  $\sim 200 \text{ cm}^{-2} \text{ nm}^{-1}$  (equivalent to  $\sim 4 \times 10^4 \text{ cm}^{-2}$  in a 200 nm film) [12].

Another way to reduce the droplet density is to place a high-speed shutter between target and substrate. Droplets are much slower than the rest of the plume (average velocity  $2 \times 10^3 \text{ m s}^{-1}$  compared to  $2 \times 10^4 \text{ m s}^{-1}$  for atoms and ions) [7], so it is possible to mechanically separate the two parts of the plasma plume. This is usually done by inserting a revolving disc between target and substrate with a window that is synchronized with the laser pulses. Depending on the deposition conditions and the filter used, droplet densities could be reduced by a factor of up to  $10^4$  [19].

When the target itself rotates while the laser is scanned over its surface, the laser beam hits the target from different angles, strongly suppressing the usual formation of cones pointing in the direction of laser incidence. Doughty et al. [20] used this fact to reproducibly deposit YBCO films with droplet densities as low as  $200 \text{ cm}^{-2} \text{ nm}^{-1}$  without having to sand or otherwise treat the target between depositions.

Some groups have tried to shield the substrate by simply putting a mask in front of it. The idea is similar to the off-axis deposition: the heavy droplets collide with the obstacle or travel outward, while the light particles can be scattered onto the substrate which is placed in the region unreachable by a direct line of flight from the target. This PLD system is called “shadow mask PLD” or “eclipse method” and can almost completely prevent droplets from reaching the substrate surface. However, the thickness of the film is usually nonuniform, and the oxygen partial pressure has a large influence on the thickness distribution, so it cannot be varied for further film optimization as is commonly done in PLD [22], [21].

Finally, droplets can be almost completely eliminated by the use of two synchronized laser beams. Two substrates are hit, producing plasma plumes which intersect at an

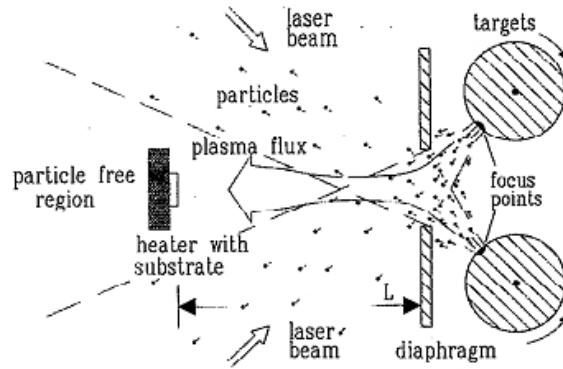


Figure 1.6: Two-beam PLD setup allowing particle-free film deposition [1].

angle of  $\sim 90^\circ$ . While the large droplets are almost unaffected by the other plume, the smaller particles get scattered, resulting in a plasma flux along the bisecting line of the two plasma plumes. This plasma flux can be used for deposition of droplet-free films (see fig. 1.6) [1].

## Propagation Phase

While expanding, the plasma plume interacts with the background gas. Depending on the background gas pressure, there are two regimes.

At pressures below about 5 Pa, the velocity of the the plasma is only slightly influenced by the background pressure [10], [28].

At higher pressures, the plume splits into two components, namely one that is not slowed by the gas and travels at vacuum speed, and one that is substantially slowed [29]. As the tip of the plume collides with the background gas and is slowed, it forms a shock wave-like contact front and coalesces with the slower-moving material [5].

The propagation of the plasma plume can best be described by a combination of a shock or blast wave model with a drag model which incorporates the viscous slowing of the plume material [30].

### 1.2.2 Layer growth

The growth mechanisms of thin films are a very complex field. To avoid going beyond the scope of this thesis, I limit myself to a short general overview over the main growth models. The interested reader is referred to “The Materials Science of Thin Films” [31] and “Pulsed laser deposition of thin films” [5] to gain a deeper insight into the science of thin film growth.

Film growth depends on many parameters, such as the rate and energy of incoming particles, the surface binding energies, surface smoothness, existence of steps on the surface, the temperature of the substrate and the background gas pressure. The growth rate itself is determined by the difference between adsorption and desorption of particles.

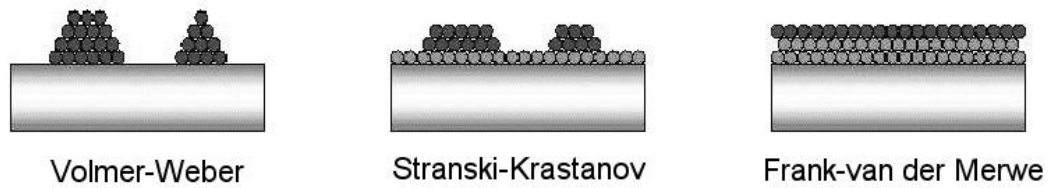


Figure 1.7: Thin film growth modes: Volmer-Weber or island growth leads to three-dimensional islands, Frank-van der Merwe or layer growth leads to flat two-dimensional layers, the intermediate Stranski-Krastanov growth leads to small clusters on completely filled layers [32].

The ratio between substrate temperature and melting temperature of the film material is decisive. A higher ratio generally leads to better crystallinity and lower growth rates: as the particles have a higher thermal energy, they move around longer before finding an energetically favorable position, but at the same time they are more prone to desorb because of their higher energy.

Three main modes of growth are generally distinguished, named layer or Frank-van der Merwe growth, island or Volmer-Weber growth and Stranski-Krastanov growth (see fig. 1.7).

These modes can be described and explained by simple thermodynamic considerations about the free energy of clusters on the surface of a substrate. Taking into account the interface energies between substrate, vapor and cluster as well as substrate temperature and supersaturation (the ratio of the pressure of the arriving atoms to the vapor pressure of the deposited material), it is possible to determine whether monolayers or clusters will form.

Although the above-mentioned growth models describe how films grow depending on the interaction between substrate and film material as well as thermodynamic parameters, the growth is often strongly influenced by the surface of the substrate itself. Dislocations and steps change local binding energies and offer favorable nucleation sites, leading to either screw dislocations or film growth through the propagation of growth steps, termed “ledge growth” [33].

### Film growth with pulsed laser deposition

In PLD, short plasma plumes lasting 5 – 10 ms are followed by long periods of hundreds of ms in which no material is deposited. The short phase of very high supersaturation allows the formation of many small clusters which are unstable at lower deposition rates due to their small size. In the intermediate period with low arrival rates, the clusters will therefore begin to dissociate and coalesce into larger, stable clusters in an Oswald ripening step. This reordering on the surface depends strongly on the kinetic energy influenced by substrate temperature.

If the second pulse arrives too quickly after the first, there will be no difference to

continuous laser deposition as no real dissociation of unstable clusters will have taken place. In the case of a long intermediate time between pulses, all the clusters will have reformed into the larger clusters that also would result from a low instantaneous deposition rate.

The film growth will only be influenced by the splitting into two phases when the time constants for the laser are such that the next pulse arrives while the atoms from the first pulse are still rearranging themselves on the surface, i.e., the laser pulses arrive on the time scale of the atomic reordering processes.

The time constants can easily be changed as most pulsed lasers allow pulse frequencies between 1 and 100 Hz without changing the pulses themselves. Therefore, the effect of different time intervals on film growth has been extensively studied, showing the expected strong influence and the existence of an optimum interval for deposition of a specific material [34].

### 1.3 Superconductivity

In 1911, Heike Kamerlingh Onnes discovered that mercury below 4.2 K has no measurable resistance [35]. Later, the Dutch physicist called the observed phenomenon superconductivity and received a Nobel prize for his research in this area in 1913. Furthermore, it was also discovered that superconductivity could be quenched by a magnetic field. Since superconductors are ideally diamagnetic, they expel any magnetic fields inside them, a property known as the Meissner -Ochsenfeld effect.

Many elements exhibit superconductivity when cooled below a certain critical temperature,  $T_C$ . Common to all superconductors is the fact that they lose the superconductive state when either the temperature is raised above  $T_C$ , or when they are immersed in a magnetic field above the critical field strength  $H_C$ , or when they carry a current above the critical current density  $j_C$ . These three parameters are directly dependent on each other as can be seen in fig. 1.8.

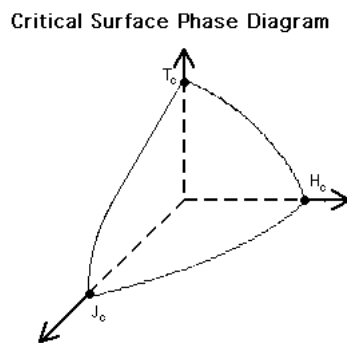


Figure 1.8: Critical surface phase diagram of Type I superconductors: the material shows superconductive behavior if it is closer to the origin than the critical surface [36].

Depending on how a superconductor becomes quenched by magnetic fields, it is classified as either Type I or Type II superconductor:

Type I superconductors are ideally diamagnetic, expelling all magnetic field until the critical field strength  $H_C$  is reached, in which case superconductivity breaks down completely. In contrast, a Type II superconductor can exist in a mixed state called Shubnikov phase [37], in which small parts of the superconductor are in normal state, allowing some flux to penetrate the material while the rest is still in superconducting state.

## 1.4 YBa<sub>2</sub>Cu<sub>3</sub>O<sub>7-x</sub>

The high-temperature superconductor YBa<sub>2</sub>Cu<sub>3</sub>O<sub>7-x</sub> (YBCO) with a transition temperature  $T_C^0 \sim 92$  K was discovered by Wu et al. in 1987 and belongs to the cuprates with perovskite-like structure. Like all high-temperature superconductors it is of Type II, with a large London penetration length  $\lambda_L$  and a short coherence length  $\xi_{GL}$ .

### 1.4.1 Crystal structure

YBa<sub>2</sub>Cu<sub>3</sub>O<sub>7-x</sub> is found in tetragonal and orthorhombic phase, depending on oxygen concentration and temperature (see fig.1.9). Only the orthorhombic phase, where  $0 < x < 0.6$ , shows superconductive behavior, and the transition temperature is highly dependent on the oxygen concentration, showing its maximum of 92 K at  $x \sim 0.05$  [38].

Superconductivity in YBCO, as in most cuprates, takes place in the CuO<sub>2</sub>-planes (assigned Cu(2) in fig.1.9): These planes are effectively hole-doped, as some electrons are transferred to the oxygen atoms in the CuO-chains (Cu(1) in fig.1.9) [39]. As the conducting CuO<sub>2</sub>-planes are only linked in a,b-direction, it is obvious that YBCO is a highly anisotropic material. The coherence length in a,b-direction is about 5-8 times larger than in c-direction, and the London penetration length  $\lambda_L$  in a,b-direction is about five times smaller than in c-direction [39].

The lattice constants of the completely oxygenated orthorhombic unit cell containing 13 atoms at room temperature can be found in table 1.1.

material	lattice parameters			volume V [Å <sup>3</sup> ]	number density n [10 <sup>22</sup> cm <sup>-3</sup> ]	thermal exp. coeff. at 300 K $\alpha_{a,b}$ [10 <sup>-6</sup> K <sup>-1</sup> ]
	a [Å]	b [Å]	c [Å]			
YBCO	3.820	3.885	11.676	173.3	7.503	10
ZnO	3.249	3.249	5.204	54.945	7.28	5

Table 1.1: Material properties of YBCO and ZnO [40], [41], [42], [43].

### 1.4.2 Growth mechanisms of YBCO thin films

The growth of YBCO thin films on various substrates via PLD has been the focus of much research for the last twenty years. Though the exact parameters vary between

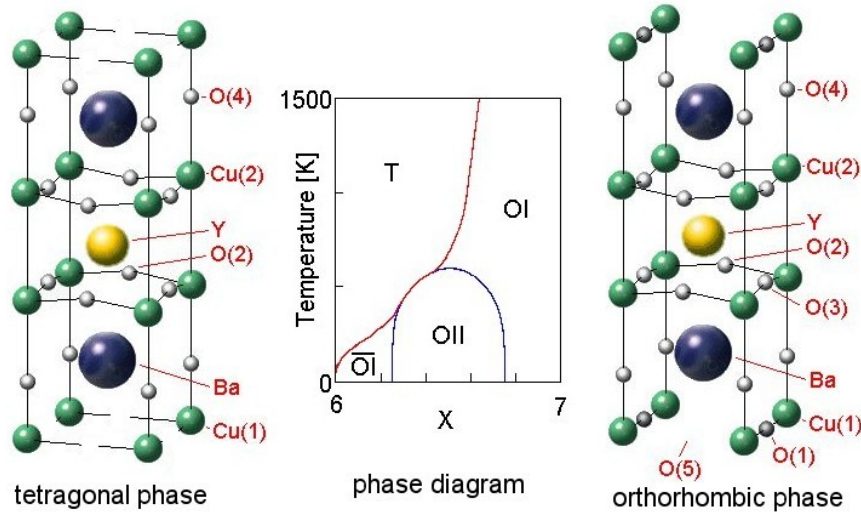


Figure 1.9: YBCO phases and phase diagram; T stands for tetragonal, O for the orthorhombic phases differing in their long-range order [44].

different groups, YBCO films are usually deposited by PLD in the following process parameter ranges [10], [34], [5]:

- oxygen pressure: between 10 and 50 Pa,
- temperature: between 650 and 850 °C,
- laser energy: between 1 and 4 J cm<sup>-2</sup>,
- laser repetition rate: between 1 and 30 Hz,
- post-deposition oxygenation oxygen pressure: 10<sup>3</sup> – 10<sup>5</sup> Pa.

While some groups claim they see proof of Volmer-Weber growth [5], the high density of relatively flat, terrace-like screw dislocations ( $\sim 10^8$  cm<sup>-2</sup>) rather supports another model, where small screw dislocations form at many nucleation sites, followed by a two-dimensional growth at the screw's step edges [33].

Chang et al. [34] found pinholes for low repetition rates around 1 Hz which they attribute to extensive nuclei ripening in the intermediate period. Higher repetition rates of 10-30 Hz improve the coalescence and lead to smooth films, while a further increase of the repetition rate yields films with precipitates, often consisting of Y<sub>2</sub>O<sub>3</sub>, YCuO<sub>2</sub> or BaCu<sub>2</sub>O<sub>2</sub>.

### Substrate Material: SrTiO<sub>3</sub>

SrTiO<sub>3</sub> (STO) is a material with perovskite structure which is commonly used as substrate for YBCO thin film deposition. Its lattice parameter in a,b-direction ( $a=b=3.905$  Å) and the thermal expansion coefficient ( $\alpha \sim 11 \times 10^{-6}$  K<sup>-1</sup>) are close to that of YBCO,

## Wurtzite (B4)

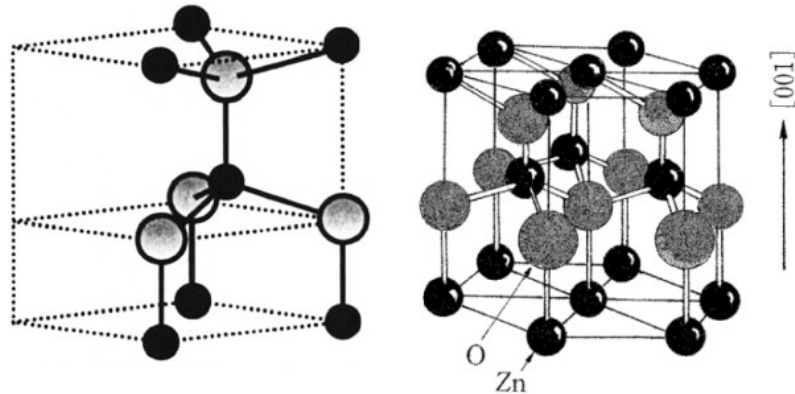


Figure 1.10: ZnO in the hexagonal wurtzite structure [2], [3].

furthermore it is chemically inert and very little diffusion is found between YBCO and STO [45], [46].

## 1.5 Zinc oxide (ZnO)

Zinc oxide (ZnO) is a wide band gap ( $\sim 3.3$  eV) semiconductor with a large free exciton binding energy of about 60 meV. ZnO single crystals are therefore transparent, while the polycrystalline target has a white-yellowish tint. ZnO is easily processed by wet chemical etching, and comparatively cheap to fabricate. Although ZnO has been known for more than fifty years, the last decade has seen renewed interest in ZnO as it seems suitable in various active fields of research like UV light emitting diodes (LED), transparent conducting oxides (TCO), surface acoustic wave guides (SAW) and lasing applications [2].

### 1.5.1 Crystal structure

ZnO forms a wurtzite structure at normal pressure, in which each zinc atom is surrounded by four oxygen atoms at the corner of a tetrahedron and vice versa (see fig. 1.10). As one basal plane terminates in zinc atoms while the other terminates in oxygen atoms, the (001) and the (00 $\bar{1}$ )-planes have different properties and the whole crystal exhibits polarity along the c-axis. This polarity explains the piezoelectric behavior and influences many properties of ZnO, including growth and etching [2].

The lattice constants of the hexagonal unit cell containing 4 atoms at room temperature can be found in table 1.1.

When grown on cubic substrates, it is possible to stabilize ZnO in cubic zinc blende



structure, while a pressure of about 10 GPa leads to a transition to rocksalt structure. The zinc blende unit cell has a lattice constant of about 4.5 Å, while the rocksalt unit cell has a lattice constant of about 4.27 Å [2].

### 1.5.2 Electric properties

Undoped ZnO shows n-type behavior with donor concentration ranging between  $10^{17}$  and  $10^{21} \text{ cm}^{-3}$ . The reason for the high charge concentration is still debated. Originally, the shallow donor levels were attributed to oxygen vacancies and zinc interstitials [2]. However, it was found that oxygen vacancies act as deep donors, and that zinc interstitials have too high formation energies to account for  $10^{17} \text{ cm}^{-3}$  free charges. It has been suggested that hydrogen is the cause for the low donor levels, a theory which is corroborated by annealing experiments [47].

Fabricating stable p-doped ZnO has long seemed impossible as the introduction of acceptors into the ZnO crystal usually resulted in overcompensation and n-type behavior, but in the last years several groups have published results which seem relatively incontrovertible [48]. They also offer explanations why many groups have not succeeded in measuring p-type doping: ZnO shows persistent photoconductivity so samples have to be protected from UV light the days before performing Hall measurements [49].

As mentioned before, the resistivity of ZnO films varies between  $10^{-4} - 10^9 \Omega \text{ cm}$ , making ZnO usable both as piezoelectric material, which requires very high resistivity, and TCO, where a very low resistivity is required [2].

### 1.5.3 Pulsed laser deposition of ZnO

Deposition of ZnO films through PLD has received considerable attention, but individual groups report very different parameters at which they produced the best films, as can be seen in table 1.2. Common to all ZnO films is the predominance of c-axis growth on most substrates. Furthermore, most groups find grain sizes of 10-100 nm, with grain size increasing as substrate temperature or oxygen pressure are increased.

To better understand the growth mechanisms of ZnO film growth, some attention has been given to the study of the plasma plume itself [8], [58].

Through high-speed analysis of the emission lines from the plasma plume resulting from ablation of ZnO with a nanosecond UV laser, different ionized states of Zn atoms together with their velocities could be observed. Usually, strong emissions from  $\text{Zn}^+$ -ions with a mean kinetic energy of 36-57 eV were found. At higher laser fluences ( $>4 \text{ J cm}^{-2}$ ) or femtosecond laser pulses, very fast  $\text{Zn}^{++}$ -ions were observed, probably fast enough ( $> 200 \text{ eV}$  kinetic energy) to damage the films.

Another feature are slow particles trailing behind the main plume, consisting probably of Zn atoms which first backscattered from the plasma and then rebounded from the target. This interpretation is corroborated by the common observation that the target surface changes upon first irradiation, even in the vicinity of the laser focus. The originally insulating yellow ZnO turns into grayish-metallic conducting material – probably a thin layer of Zn [58].

group	substrate	temperature [°C]	pressure [Pa]	$\Delta 2\theta$ [°]	$\Delta 2\omega$ [°]	roughness [nm]
Bae [50]	Al <sub>2</sub> O <sub>3</sub>	200-600	0.0001 - 67	0.2		
Beck [43]	Al <sub>2</sub> O <sub>3</sub>	300-750	0.1-40		0.45-4	0.6 - 24
Fouchet [51]	Al <sub>2</sub> O <sub>3</sub>	400-750	4 - 27		0.3 - 1.8	20 - 50
Kaidashev [52]	Al <sub>2</sub> O <sub>3</sub>	600-750	0.04 - 1.5		0.06 - 0.12	0.2 - 2
Kim [53]	Si	600	0.07 - 70	0.2 - 0.4		4 - 26
Klini [8]	Si, silica	300-650	0.005 - 0.5	0.2 - 2	1 - 9	1 - 20
Mitra [54]	glass	20	1.3 - 130	0.6 - 1.2		20 - 110
Ohshima [28]	Si, silica, Al <sub>2</sub> O <sub>3</sub>	20-700	0.007 - 27		0.5 - 8	
Prasad [55]	steel	70-80	10 <sup>-7</sup> - 0.7	0.5	10	
Savchuk [56]	quartz, Al <sub>2</sub> O <sub>3</sub>	20-550	0.13 - 1300	0.16		
Zerdali [57]	SiO <sub>2</sub>	500	0.013	0.28		

Table 1.2: Summary of deposition parameters for PLD of ZnO.

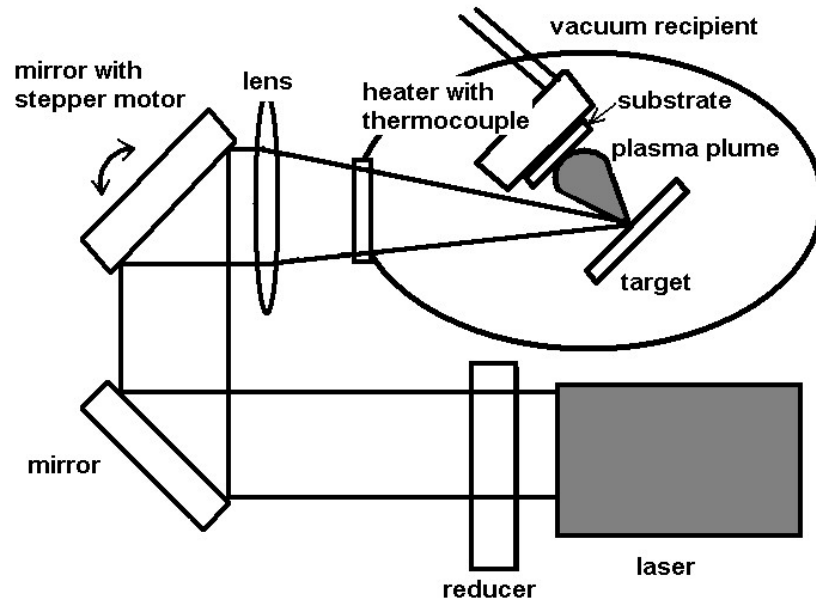


Figure 1.11: Sketch of the PLD setup in on-axis geometry.

## 2 Experimental setup: sample preparation

### 2.1 Pulsed laser deposition (PLD) setup

The basic setup of the pulsed laser deposition (PLD) System is shown in fig. 1.11.

A Lambda Physics LPX3051 KrF excimer Laser with a wavelength of 248 nm was used. The laser produced pulses with a duration of  $\sim 20$  ns at a repetition rate of 1-10 Hz. The energy could be varied between 600 and 1100 mJ per pulse.

The laser beam was focused through a lens with 50 cm focal length onto the target to a focus size of  $5 - 7 \text{ mm}^2$ . As the resulting laser intensity was too high for optimal deposition of YBCO, an optical attenuator was placed in the optical path.

The resulting laser fluence at the target was in the range of  $0.7$  to  $2.6 \text{ J cm}^{-2}$ .

Three targets (YBCO, ZnO and Au) were mounted on a revolvable target holder, with the laser beam hitting the target at an angle of about  $45^\circ$ . To improve the yield of one target, the laser spot was scanned in a rectangular pattern over the whole target surface (see fig. 2.1) with the help of a deflecting mirror controlled by two stepper motors.

As the growth of YBCO thin films requires a homogeneous substrate temperature around  $750^\circ\text{C}$ , the substrate was attached with conductive silver to a resistive heater. A thermocouple was also attached to the heater. The heating current was controlled with a Eurotherm 818P temperature control unit that used the measurement from the thermocouple to keep the temperature at a set level.

The control loop kept the temperature as measured with the thermocouple stable to  $\pm 1^\circ\text{C}$ , however, the temperature measured with the thermocouple differed widely ( $20\text{-}30^\circ\text{C}$ ) from the temperature of the substrate as determined with a pyrometer. As the pyrometer is calibrated to black-body radiation while the substrate is certainly a

**Scan pattern on target**

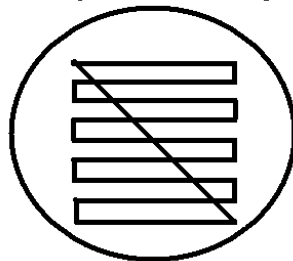


Figure 2.1: This laser scan pattern was used to maximize the yield of the target.

gray body, this effect is not surprising. Furthermore, the thermocouple is positioned about 1 cm outside the main heating area of the heater and the thermal contact between substrate and heater varies from sample to sample. For each single deposition I therefore determined the substrate temperature with a pyrometer and set the heater control loop accordingly.

From repeated measurements I determined the reproducibility of the pyrometer to  $\pm 5^\circ\text{C}$ . The accuracy of the absolute value is not known, as no suitable calibration standard was available. This uncertainty is of relatively little importance for this thesis: for an analysis of the influence of different parameters on film fabrication in this setup it suffices to have reproducible values on a relative scale, and if a transfer to another setup is wanted, it should be possible to fix this scale to the real temperature scale through an external calibration measurement.

The PLD was performed in on-axis geometry, with the substrate positioned right in front of the target with a separation of 4 cm between target and substrate.

The deposition chamber was evacuated using a Leybold Turbovac 361 turbomolecular pump with a Leybold Trivac rotary vane pump as backing pump. The minimum pressure reached with this setup was  $5 \times 10^{-5}$  Pa, measured with a Balzers compact full range pressure gage.

## 2.2 Deposition process

The substrates were first polished (rms surface roughness  $\sim 1$  nm), then cleaned in an ultrasonic bath first with acetone, then with isopropyl alcohol, blown dry with nitrogen, and finally wiped clean with acetone-moistened wipes.

The substrates were glued onto the heater with conductive silver paste to ensure uniform heat transport from heater to substrate and therefore even heating of the substrate.

First, the vacuum recipient was evacuated to less than  $3 \times 10^{-4}$  Pa. The turbomolecular pump was then switched off and the oxygen flow was increased until the deposition pressure for YBCO was reached (10-40 Pa with rotary vane pump still running). While the substrate was protected by a mask, the target was ablated for a minute (about 10 shots per site).

The substrate was heated to the deposition temperature (700-850 °C), and the YBCO deposition was performed. Then, the rotary vane pump was stopped and the oxygen pressure increased to  $6 \times 10^4$  Pa. The temperature was decreased down to room temperature at a rate of 2400 °C/hour.

In the case of subsequent ZnO deposition, the vacuum recipient was then evacuated with the rotary vane pump down to 0.3 Pa before the oxygen flow was increased to reach the desired pressure (1-10 Pa with rotary vane pump still running). The deposition temperatures were lower than the ones for YBCO (200-550 °C), but else the deposition process and parameters were the same.

I am aware of the fact that the changing pumping speeds of the rotary vane pump at different pressures together with the positioning of the pressure meter to the side of the oxygen inlet decrease the accuracy and validity of the pressure measurements. However,

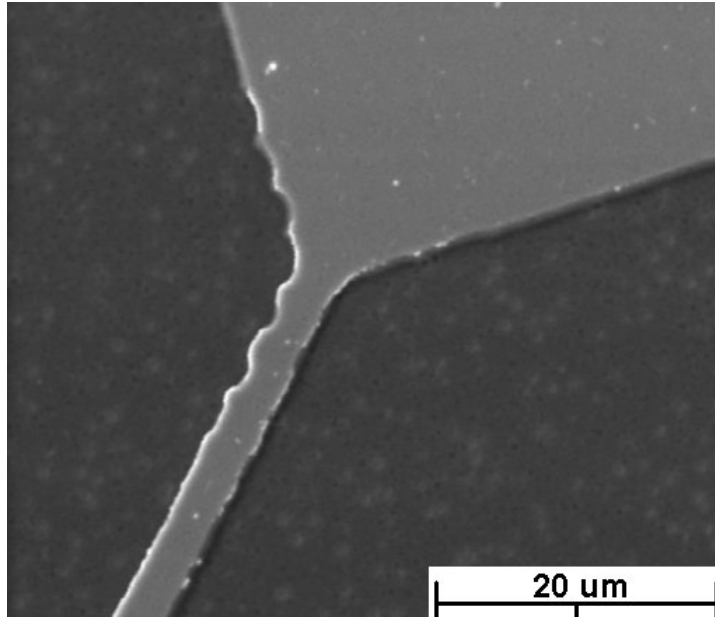


Figure 2.2: Ion-etched  $j_C$ -bridge (SEM picture, SE mode).

no gas flow meter was available to directly meter the gas flow. Therefore, the given figures for the oxygen pressure should be used with care. A comparison of plasma plume size at a given laser energy between the vacuum system used for this thesis and another vacuum system in the same laboratory may serve as an example. To reach a similar plume size as seen in recipient 1 at an oxygen pressure of 10 Pa, the pressure in recipient 2 had to be set to 30 Pa.

### 2.3 Patterning of the YBCO films

For measurements of the critical current density of YBCO, the YBCO films had to be patterned into thin bridges (2-20  $\mu\text{m}$  wide, 0.5 mm long) with two gold bond pads at each side for four-point measurements. This was done by sputtering, photolithography and ion etching.

The edges of YBCO film were first sputtered with a 200 nm gold layer to later allow bonding for electrical readout. The whole film was then spin-coated with  $\sim 2 \mu\text{m}$  of a UV-sensitive positive photoresist. The photoresist layer was exposed to UV light through a chrome mask covering the bridge and the bond pads, then the exposed photoresist was developed and washed away. The sample was then ion-etched with  $\text{Ar}^+$ -ions until only the covered YBCO bridges and gold bond pads remained.

An SEM picture of the resulting  $j_C$ -bridges can be seen in fig. 2.2.

## 3 Analytical methods

To determine the properties of the fabricated layers, several analytical methods were used. The properties and the respective methods are shown in table 3.1 and detailed below.

Property	Method
surface morphology	Atomic Force Microscopy (AFM) Scanning Electron Microscopy (SEM)
layer thickness	Dektak profilometer Rutherford Backscattering Spectroscopy (RBS)
crystallinity	X-Ray Diffraction (XRD)
superconducting properties: $T_C^0$ $j_C$	R(T) measurements I-V characteristics

Table 3.1: Analyzed properties and the respective analytical method

### 3.1 Profilometry

The thickness of the YBCO layers was determined with the help of a Dektak 3030 profilometer. Parts of the YBCO film were wet etched with 3% hydrochloric acid (HCl) to create a sharp step edge between film and substrate. Although the resolution of the profilometer was stated as 0.1 nm, the film thicknesses could only be measured to an accuracy of  $\pm 15$  nm due to film roughness and rounding effects at the step edge.

### 3.2 Rutherford backscattering spectroscopy (RBS)

Rutherford Backscattering Spectroscopy (RBS) relies on the wide-angle scattering of light ions (usually  $\text{He}^+$  or  $\text{H}^+$ ) with high kinetic energies in the range of 100 keV to some MeV on target atoms inside a solid.

An ion beam is focused onto a target and the amount and energy of the backscattered ions are measured by a detector. The ions mostly undergo elastic scattering with the atoms in the sample, so the energy of the backscattered ion is directly dependent on the mass of the nucleus. Therefore, elements on the surface of a sample can be identified by the energy of backscattered ions.

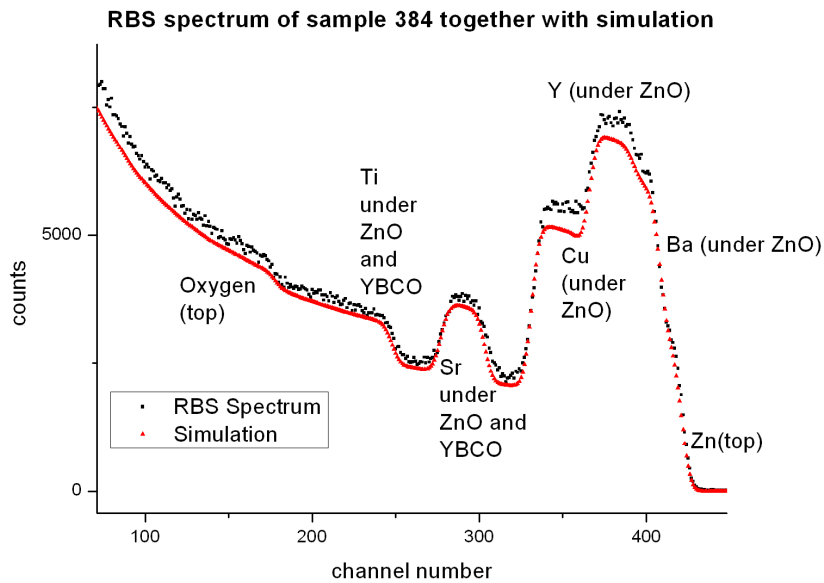


Figure 3.1: Measured RBS spectrum of a sample, together with a simulation of 145 nm ZnO on 235 nm YBCO on STO.

The energy of the scattering ions is so high that many penetrate deeper into the sample, undergoing both low-angle elastic and inelastic scattering, thereby losing energy. When these ions finally undergo wide-angle scattering back into the detector, they have a lower energy than if they had scattered on the same element at the sample surface. Accordingly, the energy of a detected ion depends on both the mass of the scattering atom and the depth at which it got backscattered.

Using numerical analysis tools, it is possible to fit an RBS spectrum to extract the thickness and stoichiometric composition of individual layers of a multi-layer system. However, as both pieces of information are extracted from one single parameter, a certain knowledge of expected elements is needed for the interpretation of the rather complicated spectra of multi-layer systems.

A sample spectrum together with the fit can be seen in fig. 3.1.

The measurements to determine layer thickness and stoichiometry were taken in *random mode*, in which the crystal is tilted by about  $5^\circ$  so the chance of a specific crystal orientation being perpendicular to the incoming ion beam is minimized. For further information, the reader is referred to the book “High Energy Ion Beam Analysis” [59]

### 3.3 Atomic force microscopy (AFM)

Atomic force microscopy (AFM) was developed in 1986 by Binnig, Quate and Gerber and uses molecular forces to map the surface of a sample: in contact mode, the apex

atom of a tip is scanned over a surface and experiences a repulsive force when coming too close to the surface atoms. As the tip is mounted on a flexible cantilever, the force leads to a deflection of the cantilever which is monitored with a laser. A feedback-loop moves the cantilever with the help of piezoelectric ceramics so that the tip always experiences the same repulsive force from the surface. In principle, an AFM can reach a sub-nm lateral and even better vertical resolution. Further information can be found in the book “Surface analysis with STM and AFM: experimental and theoretical aspects of image analysis” [60].

The AFM pictures shown in this thesis were taken with a Veritekt AFM by Zeiss, reaching a resolution of  $\sim 5$  nm in lateral and  $\sim 0.5$  nm in vertical direction. All root-mean-square (rms) roughnesses were determined over an area of  $5 \times 5 \mu\text{m}^2$ .

### 3.4 Scanning electron microscopy (SEM)

Scanning electron microscopy (SEM) uses the scattering of high-energy electrons on a sample to reveal topographical and material-sensitive information about the surface. Electrons are accelerated to kinetic energies of 10-30 keV and focused through a series of electromagnetic lenses onto the target. The fast electrons impinge on the surface and undergo elastic and inelastic scattering in the first few nm, either creating cascades of secondary electrons with much lower kinetic energy or backscattering from a nucleus, thereby retaining their energy but changing the direction. The electron beam is scanned over the sample and either the low-energy secondary electrons (SE mode) or the high-energy backscattered electrons (BSE mode) are measured by a detector. While the amount of secondary electrons depends mainly on the topography, the amount of backscattered electrons depends strongly on the element: the heavier the nucleus, the higher the number of backscattered electrons. Further information can be found in the book “Physical principles of electron microscopy” [61].

The SEM pictures shown in this thesis were taken with a TESLA BS 343 SEM, reaching a lateral resolution of  $\sim 100$  nm.

### 3.5 R(T)-measurements

To determine the critical temperature  $T_C^0$  of the YBCO thin film, simple four-point probe resistance measurements were taken. The four contacts made from copper wire were mechanically pressed onto the YBCO surface, while the back of the substrate touched a large brass body which acted as a thermal mass. A platinum thermocouple (Pt100) was fixed to this brass body to monitor the temperature. A DC current of  $100 \mu\text{A}$  was supplied by a constant current source while the voltage drop on the other two electrodes was measured with a Prema 5000 Digital Multimeter. The sample was slowly lowered (about 20 K per hour in the region of 77.4-100 K) by a stepper motor into a dewar with liquid nitrogen while the resistance and the temperature were registered by a computer. A sample R(T)-curve can be seen in fig. 3.2.



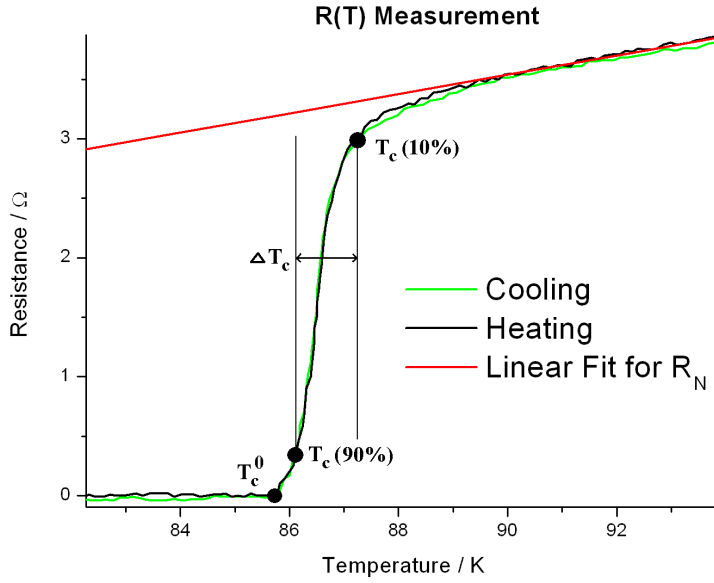


Figure 3.2: Sample  $R(T)$ -measurement of an YBCO film, showing  $T_C^0$ ,  $T_C(90\%)$  (temperature at which the resistance dropped by 90% of the linear fit of the normal resistance),  $T_C(10\%)$  and  $\Delta T_C = T_C(10\%) - T_C(90\%)$ .

The definition of the critical temperature  $T_C$  of the transition from normal to superconducting state varies in literature [37]. In this work, the following terms are used (see fig. 3.2 for visualization):  $T_C^0$  (temperature at which the resistance dropped to zero within the measurement accuracy of  $\Delta R \sim 0.05 \Omega$ ),  $T_C(90\%)$  (temperature at which the resistance dropped by 90% of the linear fit of the normal resistance),  $T_C(10\%)$  (temperature at which the resistance dropped by 10% of the linear fit of the normal resistance) and  $\Delta T_C = T_C(10\%) - T_C(90\%)$ .

To judge the reliability of the measured values and to estimate the influence of the rate of temperature change, measurements were taken both while lowering and while raising the sample, thereby decreasing and increasing the temperature. Although differences in  $T_C^0$  of up to 4 K were found at higher rates of temperature change, no difference was noted for measurements taken with the above-mentioned rate of  $\sim 20$  K per hour.

The accuracy of the determination of  $T_C^0$  depends strongly on the  $R(T)$ -curve. While some samples showed a very abrupt transition in which the maximum uncertainty would be  $\pm 0.25$  K, other samples showed a strong tail in the transition which increases the uncertainty to  $\pm 1.5$  K. The same holds for the accuracy of  $\Delta T_C$ : the determination of  $T_C(10\%)$  is difficult as the upper shoulder of the  $R(T)$  curve tends to be quite round.

Note that four-point probe resistance measurements show zero resistance as soon as there is a superconducting path between the contacts. For information about larger areas of the layer other methods like magnetic susceptibility measurements are more suitable.

## 3.6 $j_C$ -measurements

The critical current density  $j_C$  was determined by measuring I-V characteristics of structured micro-bridges (0.5 mm long and 2-20  $\mu\text{m}$  wide) at 77.4 K with a Keithley source measure unit. The critical current was determined by the 10  $\mu\text{V}$  criterion. The main uncertainties arise from the film thickness (known to  $\pm 10\%$ ) and the bridge width (known to  $\pm 0.5 \mu\text{m}$ ).

## 3.7 X-ray diffraction (XRD)

For the last century, X-Ray Diffraction (XRD) methods have been the most important and powerful tool for the analysis of crystallography. XRD is based on the fact that the wavelengths of X-rays are in the order of magnitude of the separation of single atoms or molecules in solids, i.e., 0.05-5 nm. Therefore, X-rays undergo diffraction in an ordered solid, leading to reflexes according to Bragg's law [4]:

$$n\lambda = 2d \sin \Theta, \quad (3.1)$$

where  $n$  is the order of the reflex,  $\lambda$  the X-ray wavelength,  $d$  the lattice plane spacing, and  $\Theta$  the angle between incident X-ray and lattice plane.

It is possible to extract information about lattice spacing, crystallite size, out-of-plane orientation and in-plane orientation from the X-ray diffraction data, as will be explained later in more detail.

### 3.7.1 X-ray diffractometer

The set-up used for my experiments was a Seifert Bragg-Brentano-diffractometer (see fig. 3.3) with a four-circle goniometer for sample positioning. The four-circle goniometer allows independent control of  $2\Theta$ ,  $\omega$ ,  $\chi$  and  $\phi$  (see fig. 3.4 for a visualization of these angles).

The X-rays were produced with a copper anode, and a bent graphite crystal was used as monochromator, reflecting only the copper  $K_{\alpha 1}$ -line with a wavelength of 1.5404  $\text{\AA}$  and - slightly weaker but still visible - the copper  $K_{\alpha 2}$ -line at 1.5444  $\text{\AA}$  (see fig. 3.5 for a sample X-ray diffractometer chart). The strong substrate reflexes show additional peaks at lower  $2\Theta$  values. If these peaks are attributed to the known lattice spacings, X-ray wavelengths of 1.475  $\text{\AA}$  and 1.392  $\text{\AA}$  can be calculated, hinting at tungsten ( $L_{\alpha 1} \sim 1.4764 \text{\AA}$ ) and copper ( $K_{\beta 1} \sim 1.3922 \text{\AA}$ ) as the source of these reflexes [62]. The tungsten line is not surprising since the cathode is made from tungsten and the diffractometer is quite old, so some contamination of the anode with tungsten is to be expected.

### 3.7.2 Lattice spacing and crystallite size

To determine the lattice spacing, an  $\omega - 2\Theta$ -scan is taken, in which  $2\Theta$  is increased twice as fast as  $\omega$ . From the  $2\Theta$  value of a reflex together with the wavelength of the X-rays used it is easy to calculate the lattice spacing from Bragg's law, eq. (3.1).

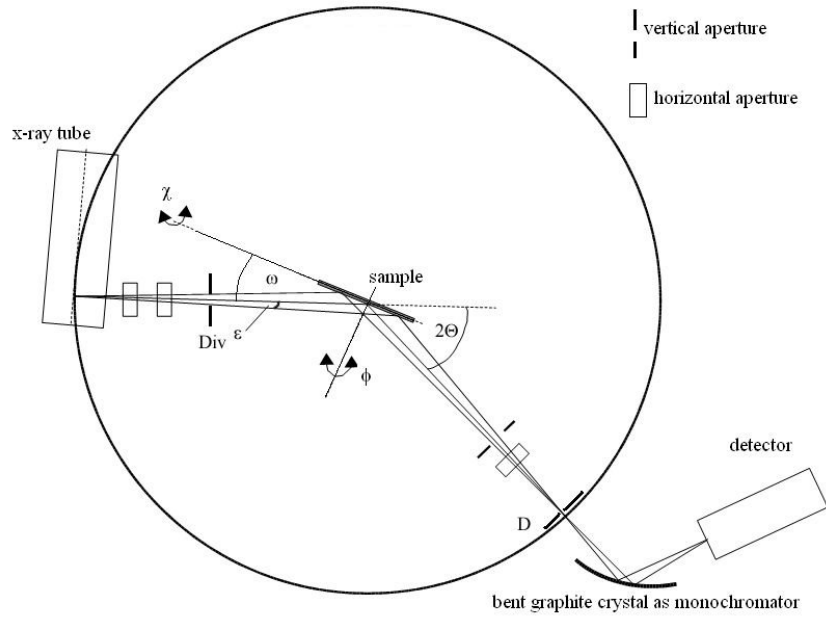


Figure 3.3: Sketch of the Bragg-Brentano X-ray diffractometer with a four-circle goniometer.

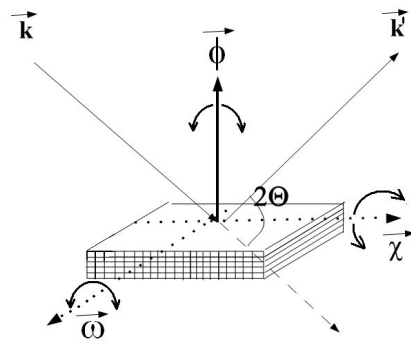


Figure 3.4: The angles accessible by the four-circle goniometer:  $2\theta$ ,  $\omega$ ,  $\chi$  and  $\phi$ .

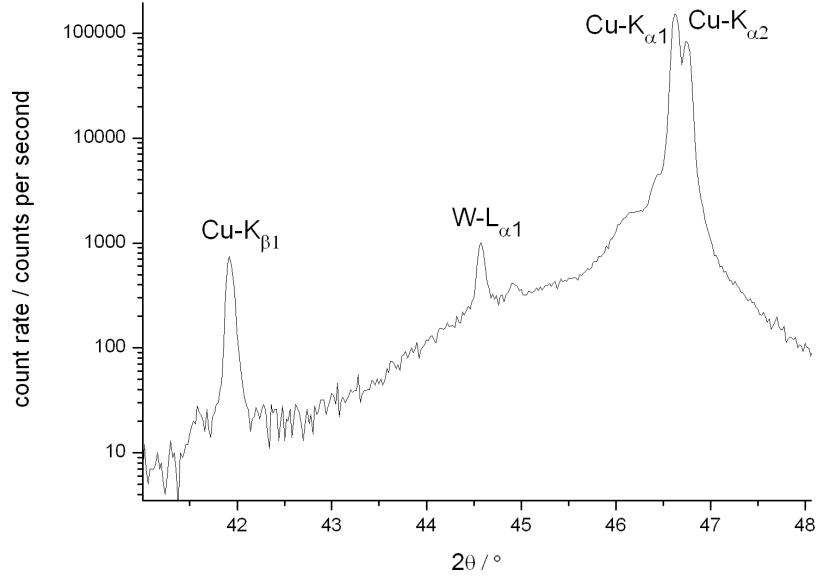


Figure 3.5: XRD chart, showing the multiple reflexes from the  $\text{STO}_{002}$  peak due to different X-ray lines.

To compensate for a possible systematic offset of the measured  $2\Theta$  values, I also measured  $2\Theta$  of the (001) and (002) peak of the STO substrate. Compared with the calculated lattice spacing values for STO the  $2\Theta$  values are  $0.18^\circ$  too large, so I subtracted  $0.18^\circ$  from all further  $2\Theta$  measurements.

An infinite perfect crystal would result in a perfectly narrow reflex, however real crystallites are finite, smearing out the Bragg reflex. It is therefore possible to calculate the crystallite size from the full width at half maximum (FWHM) of a peak in the  $\omega - 2\Theta$  scan,  $\Delta_{2\Theta}$ , according to the Debye-Scherrer-Formula [4]:

$$\langle L \rangle = \frac{K\lambda}{B_{1/2} \cos \Theta}, \quad (3.2)$$

where  $L$  is the crystallite column length perpendicular to the surface averaged over the film volume,  $K$  the Scherrer constant (depending on the unit cell geometry, typically between 0.8 and 1.4) [63],  $B_{1/2}$  the FWHM of the peak in radians and  $\Theta$  the Bragg angle for the peak.

Beside the crystallite size there are other reasons for peak broadening like the above-mentioned diffractometer broadening or strain broadening, so this formula should only be used to give the order of magnitude of the crystallite size, not exact values.

As the Scherrer constant is determined by the geometry of the crystallites which is usually unknown, it is commonly set as unity. Consequently, the values calculated in this work should be treated with caution, and an uncertainty of  $\pm 50\%$  is estimated.

### 3.7.3 Crystal orientation

The out-of-plane orientation can be determined through an  $\omega$  rocking curve.  $2\Theta$  is fixed to the value of the analyzed reflex while  $\omega$  is varied. The FWHM of the rocking curve,  $\Delta_\omega$ , is a common measure for how well the crystallites are oriented with respect to the substrate normal.

A misalignment of the out-of-plane orientation of two consecutive layers can be found by first measuring the offset between  $\omega$  and  $\Theta$  of one layer and then comparing it with the offset of the second layer.

To determine the in-plane orientation, it is necessary to do an asymmetric scan to plot the reflex of a lattice plane which is not parallel to the substrate. To this end, the angle between lattice plane normal and substrate normal has to be calculated according to eq. (1.3) for orthorhombic crystals and eq. (1.4) for hexagonal crystals.  $\chi$  is set to this angle,  $2\Theta$  and  $\omega$  are set to their respective values, and  $\phi$  is scanned from 0 to 360°.

The FWHM values of the  $\phi$ -scan is a common measure for the in-plane orientation. As it is much easier to overlook an asymmetric peak due to the additional degrees of freedom, all  $\phi$ -scans were recorded with the largest aperture.

Asymmetric scans can also be used to detect the growth orientation, e.g., a-axis growth in YBCO. Usually, a-axis growth would be detectable through a simple  $\omega$ - $2\Theta$ -scan, but the strongest a-axis peak at 47.49° is completely overshadowed by the STO substrate peak at 46.6° which has wide flanks. Therefore, it is necessary to use a peak like YBCO<sub>102</sub> which is not parallel to the c-axis (offset by 56°), fix  $\omega$  and  $2\Theta$  to the corresponding values and do  $\phi$ -scans at  $\xi=56^\circ$  and  $\xi=90^\circ-56^\circ=34^\circ$ . If a peak appears at  $\xi=56^\circ$ , the film has c-axis oriented grains, if a peak appears at  $\xi=34^\circ$  there are also a-axis oriented grains.

### 3.7.4 Evaluation of the XRD data

The XRD data results from the convolution of a Gaussian resulting from “diffractometer broadening”, mostly due to the aperture size, with the actual curve stemming from the diffraction process, which in itself may have the form of a Gaussian (e.g. due to limited crystallite size) or a Lorentzian, the natural line shape of any exponentially dampened transition.

As the natural line width is smaller than either the broadening due to aperture size or due to crystallite size, the resulting curve “final” is here presumed to be the convolution of two Gaussians “initial” and “broadening” with individual full width at half maximum (FWHM)  $\Delta_{\text{initial}}$  and  $\Delta_{\text{broadening}}$ , leading to a combined FWHM  $\Delta_{\text{final}}$  according to

$$\Delta_{\text{final}} = \sqrt{\Delta_{\text{broadening}}^2 + \Delta_{\text{initial}}^2}. \quad (3.3)$$

The initial line width can therefore easily be calculated if the diffractometer broadening is known. Due to the quadratic terms, this correction is only necessary for FWHM

values smaller than three times the diffractometer broadening; for larger initial FWHM values the broadening influence is below 10 %.

To evaluate the XRD data, the program “Analyze” supplied with the diffractometer was used. The  $\omega$ - $2\Theta$ -scans were fitted with multiple Gaussian curves, yielding position and full width at half maximum (FWHM) for each peak. The rocking curves, which have the form of a Voigt curve<sup>1</sup>, were fitted with a Pseudo-Voigt, which is just a linear combination of a Lorentzian with a Gaussian.

### 3.7.5 Accuracy of the measurements

The accuracy of the measurements is determined by several factors.

For the position, accuracy of the  $2\Theta$  measurement and the positioning of the sample are of importance. The specifications of the X-ray diffractometer give the accuracy of the angles as  $\pm 0.005^\circ$ . The influence of sample position on  $2\Theta$  can easily be seen in fig. 3.3: if the sample is behind the middle of the circle, the actual angle of diffraction is larger than the one calculated from the position of source and detector. The sample position was determined through a contact gage to  $\pm 0.02$  mm, from which an uncertainty of  $\pm 0.004^\circ$  can be calculated for a  $2\Theta$ -range of 30 to  $50^\circ$ .

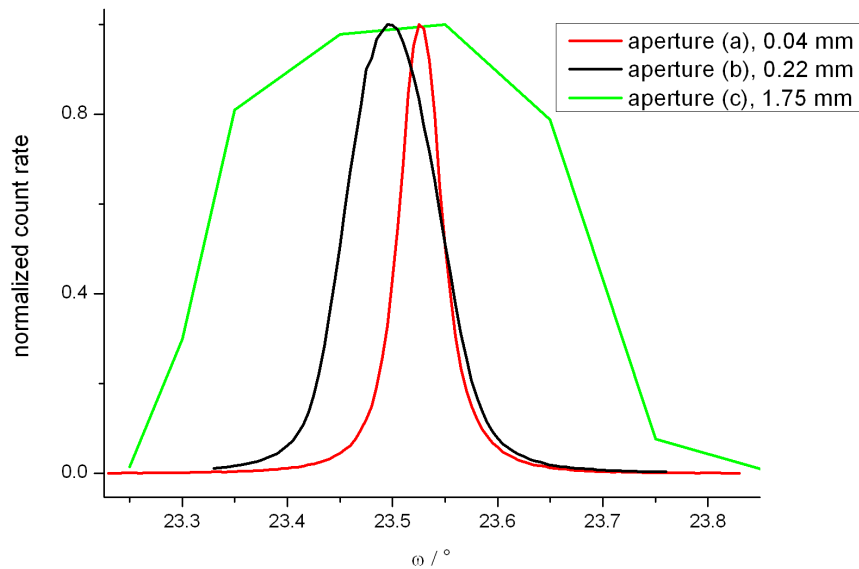


Figure 3.6: XRD chart: rocking curves of the  $\text{STO}_{002}$  peak measured with different apertures showing different FWHM values and an offset for aperture (a). Note that the shift of the peak position observed for aperture (a) has no effect on the data evaluation, as this aperture was only used to determine the FWHM of rocking curves.

<sup>1</sup>A Voigt curve is the convolution of a Gaussian with a Lorentz curve.

However, the peak position is determined through a fit of the XRD data with a Gaussian. The accuracy of the fit itself is limited by the aperture size and amount of statistical noise. A smaller aperture improves the accuracy, but also reduces the count rate, increasing statistical noise for samples with low crystallinity.

The minimal FWHM measurable with different apertures was experimentally determined by measuring the rocking curve of the STO single crystalline substrate which is expected to have a natural line width far below the resolution capability of this diffractometer. The resulting FWHM are  $0.045^\circ$  for aperture (a) (0.04 mm),  $0.09^\circ$  for aperture (b) (0.22 mm), and  $0.4^\circ$  for aperture (c) (1.75 mm) in fig. 3.6). For this thesis, most scans were taken with aperture (b), only for measurements of rocking curves with FWHM below  $0.14^\circ$  aperture (a) was used, and for asymmetric scans (see chapter 3.7.3) aperture (c) was used.

The accuracy is strongly diminished by the fact that the peak itself often does not have the form of a Gaussian or even a Pseudo-Voigt, but rather has a shoulder to the right side which might be the result from the Cu  $K_{\alpha 2}$ -reflex. Therefore, an uncertainty of  $\pm 15\%$  of the FWHM of a fit is assumed both for position and FWHM of a peak. As this uncertainty is usually larger than the uncertainties arising from sample positioning and  $2\Theta$ -measurement, these  $\pm 15\%$  of FWHM are taken as the final uncertainty for all XRD values.

## 4 Experimental results and discussion

In this thesis, a separation of the presentation of results and their discussion was overruled in favor of a joint approach, treating each property like variation of film surface in dependence of deposition parameters in itself, before continuing with the next aspect, e.g., crystallinity.

For the fabrication of thin film multilayer epitaxial structures, both surface and morphology of the individual layers are of utmost importance.

If the surface of a layer is too rough or covered by droplets, the next layer will not evenly cover it. When the surface roughness is in the order of magnitude of the film thickness (50-100 nm), the electrical properties will be unpredictable in a multilayer system, and the same is true for a droplet with a size of 0.5-2  $\mu\text{m}$ : it is immediately obvious that a droplet in the active area of a device may lead to an electrical short-circuit, rendering the multilayer structure useless.

The crystal structure needs to be well-oriented, else epitaxial growth of consecutive layers becomes impossible.

Therefore, the layers were optimized towards minimum surface roughness, minimum droplet density and best out-of-plane orientation. The YBCO layers need to be improved towards better superconducting properties, but in this thesis this task was subordinate to the achievement of multilayer structures and awaits completion by later graduate students.

### 4.1 Changes to the pulsed laser deposition system

#### 4.1.1 Target treatment

As described in chapter 1.2.1, the target surface deteriorates in the PLD process. In fig. 4.1, pictures of the target surface before and after deposition are shown.

To reduce the number of droplets and prevent a change in laser absorption through cone formation, the target was sanded after each single deposition, thereby returning the surface to its virgin state. As the composition of the top layer of the target is quickly changed by the first laser shots, the target was ablated for a minute (about 10 shots per site) before deposition to ensure a relatively uniform target composition over the course of one deposition.



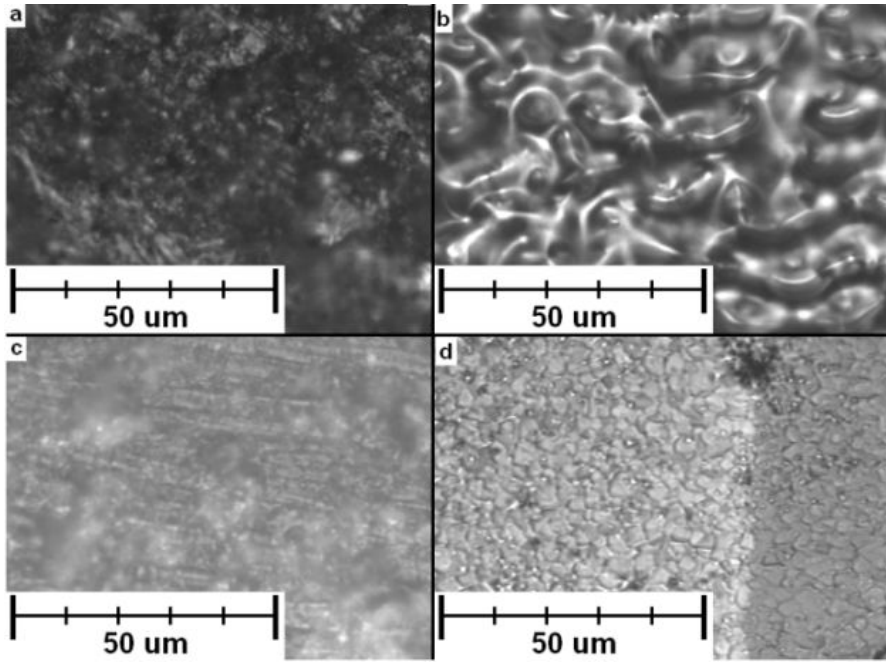


Figure 4.1: Target surface (OM pictures): a) YBCO before deposition b) YBCO after deposition c) ZnO before deposition d) ZnO after deposition.

### 4.1.2 Laser focus

To determine the size of the laser focus, thermal paper was fastened to the target and hit by a single laser pulse.

As seen in fig. 4.2a, the main maximum becomes oval and secondary maxima appear when the laser beam is focused to its maximum intensity. Furthermore, the laser intensity seems to vary over the area of the main maximum, although both the spatial and the energy density resolution of the thermal paper are not sufficient for a quantitative analysis.

Observation of the target shows melting in the close vicinity of the main maximum (see fig 4.3). As explained above, melting of the target without evaporation increases droplet formation, so it was necessary to change the optical path and the laser focus.

The laser beam leaving the laser has a cross-section area of  $1.6 \times 3.2 \text{ cm}^2$  and consists of one strong beam and two secondary beams which propagate at a small angle to the primary beam, leading to the two secondary maxima seen in fig. 4.2a. To remove these secondary beams, the optical path was extended to about three meters by inserting two high-reflectivity mirrors. The secondary beams now passed to the side of the final mirror, so only the main beam was focused by the lens onto the substrate. This led to a decreased energy, but it improved the beam profile.

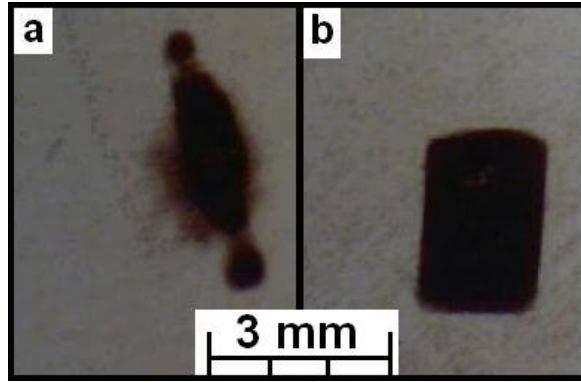


Figure 4.2: Photographs of laser focus at target site: a) old laser focus on thermal paper b) new laser focus on thermal paper.

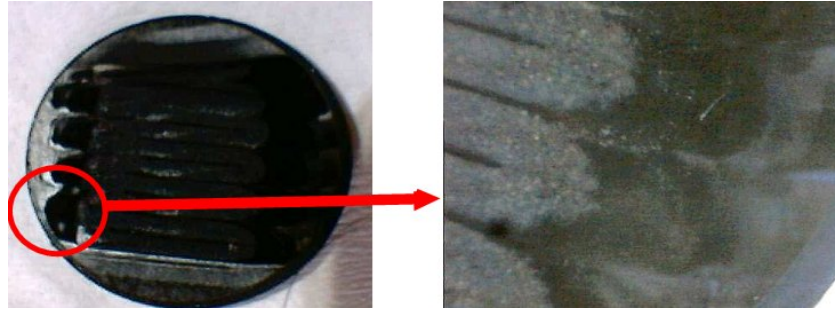


Figure 4.3: Photos of YBCO target after deposition: melting outside the directly ablated areas [14].

The optimal focus was then determined to be 1 cm behind the focal point (focal length of the lens: 50 cm). The resulting focus has a rectangular form with relatively sharp edges (see fig. 4.2b). As the target is at a  $45^\circ$  angle to the incoming laser beam, the size of the rectangle varies between  $(5.25 \pm 0.2) \text{ mm}^2$  and  $(7.05 \pm 0.2) \text{ mm}^2$ , depending on whether the target is hit at the top or the bottom. The average focus size of  $6.15 \text{ mm}^2$  was taken to calculate laser fluence values, and the change of focus size by  $\pm 0.9 \text{ mm}^2$  (relative variation of 15%) together with a laser stability of  $\sim 5\%$  leads to a variation of the laser fluence of  $\sim 20\%$ .

The laser fluences used for film deposition were  $(1.8 \pm 0.4) \text{ J cm}^{-2}$ ,  $(1.05 \pm 0.21) \text{ J cm}^{-2}$  and  $(0.93 \pm 0.19) \text{ J cm}^{-2}$ .

As most of the better films were made at a laser fluence close to  $1 \text{ J cm}^{-2}$  which is often stated as a lower bound for YBCO PLD, the fluence variation due to the scanning of the target may actually have an influence on the YBCO films. However, the geometry of the PLD setup makes it impossible to overcome this angle-dependant resizing of the focus: to hit the target at the steeper angle necessary for a more uniform focus size, the laser beam would have to pass through the substrate heater which has to be positioned right in front of the target for on-axis PLD.

### 4.1.3 Droplet density

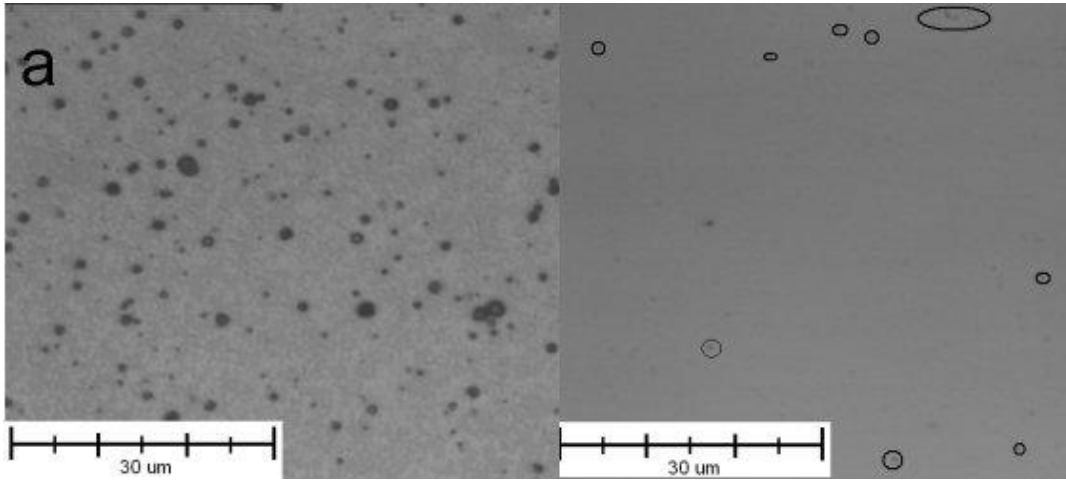


Figure 4.4: Droplet densities (OM pictures) a) YBCO film made with old PLD setup, showing high droplet density b) almost droplet-free YBCO film after change of PLD setup (microscope artifacts encircled).

The combination of sanding the target before each PLD process and refocusing the laser lead to a major decrease of droplets, as shown in fig. 4.4. The films made before the change have droplet densities around  $3 \times 10^6 \text{ cm}^{-2}$ ; in contrast, the newer films have average droplet densities as low as  $5 \times 10^4 \text{ cm}^{-2}$ .

To analyze the droplet densities,  $60 \times 80 \mu\text{m}^2$  pictures were taken with an optical microscope (OM), the fastest method to get an impression of the surface. While on the OM pictures even the new films seem to show many droplets debris, most of the observed objects are artifacts produced by the microscope itself. For clarification, the artifacts in the picture of the smooth film are emphasized by circles. Separation between real objects and artifacts is easily done on a computer screen by fast flicking between two pictures taken at the same session - the artifacts stay at the same position, while the real objects shift.

The separation between droplet and precipitate is too difficult to ensure reliable statistics. Therefore, films with precipitates (recognizable through a highly regular spatial distribution of objects) were not included for the determination of droplet densities.

For the pictures it was necessary to chose areas where some droplets were visible as some contrast was needed to focus the microscope. Therefore all pictures show at least a few droplets, although there were also areas on the films without any droplets at all. When averaging the counted droplets over fifteen smooth films without precipitates, a droplet density of  $10^5 \text{ cm}^{-2}$  resulted.

However, six smooth YBCO films were analyzed with an SEM, allowing the scanning of a larger region ( $105 \times 105 \mu\text{m}^2$ ) with a contrast high enough to still detect all droplets. Based on these images (see fig. 4.5), average droplet densities of  $5 \times 10^4 \text{ cm}^{-2}$  (film surface) or  $250 \text{ cm}^{-2} \text{ nm}^{-1}$  (film volume) were calculated. At this droplet density, the films are

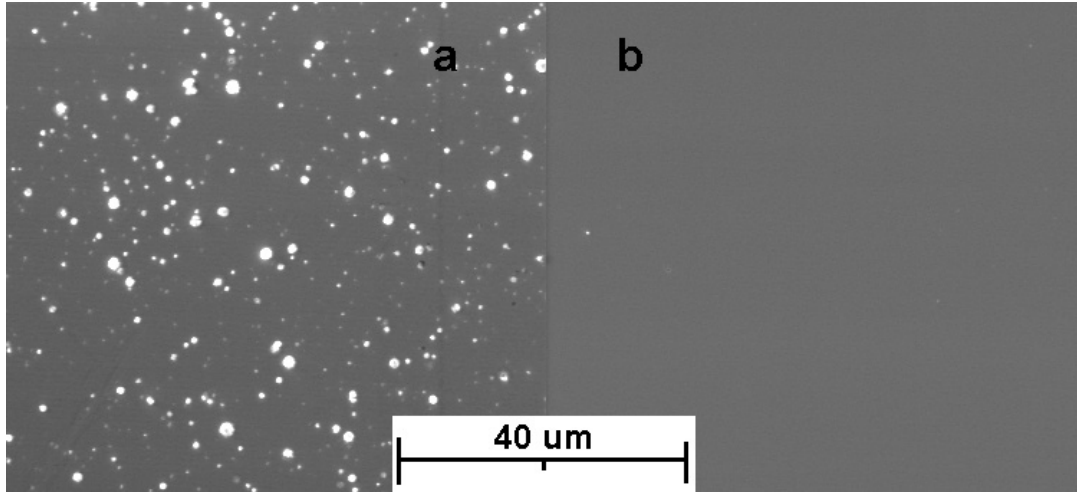


Figure 4.5: Droplet densities (SEM pictures, SE mode) a) YBCO film made with old PLD setup, showing high droplet density b) almost droplet-free YBCO film after change of PLD setup.

well-suited for further use in multi-layer processing: the chance of finding a droplet in the active area of a micro-electronic device (e.g., a SQUID) which usually have sizes of  $10 - 100 \mu\text{m}^2$  is reduced to less than 1:20.

When comparing this result with other YBCO films produced by on-axis PLD having average droplet densities of  $10^6$ - $10^7 \text{ cm}^{-2}$  [23], [26], or with the works of Schmauder et al. [27] who did off-axis-deposition with the same PLD setup and found their lowest droplet density of  $3 \times 10^5 \text{ cm}^{-2}$  at an angle of  $60^\circ$  between target and substrate<sup>1</sup>, I was able to significantly reduce the number of droplets.

Other groups have used different methods to lower their droplet densities even further, as was discussed in chapter 1.2.1. However, if the setup cannot be changed for either financial or technical reasons, the techniques used in this thesis seem a feasible option to greatly reduce droplet densities to the point where resulting films can be used for microelectronic devices without having too many droplet short-circuits.

#### 4.1.4 Heater

To simplify the deposition process and reduce contamination by conductive silver paste, I experimented with a new clamping heater design.

Usually, the substrates are glued to the heater with conductive silver, making the exchange of substrates a lengthy process: the old substrate is carefully removed with a blade (thin substrates may break when glued too tightly to the heater), the heater surface is sanded to remove the old conductive silver paste, new silver is applied, the substrate is pressed into the silver, the heater is slowly heated over 30 min first to  $110^\circ\text{C}$  and then to  $300^\circ\text{C}$  to let the solvent slowly evaporate, because faster heating leads to

<sup>1</sup>At  $0^\circ$  degree (on-axis) they report a droplet density of  $1.5 \times 10^6 \text{ cm}^{-2}$ .

bubble formation and therefore uneven heat transfer between heater and the back side of the substrate.

Furthermore, the back of the substrate is covered in conductive silver paste after deposition. When the substrate is cleaned in an ultrasonic acetone bath for further processing steps, small silver particles are often swept onto the YBCO surface, possibly leading to short-circuits in multi-layer systems [64].

The new clamping system was designed to facilitate the exchange of substrates and avoid the use of conductive silver paste: using a mask which covered only the outer half millimeter of the substrate, the back of the substrate was pressed to the smoothed surface of the heater to form a good thermal contact between heater and substrate. While it was possible to achieve sufficiently high substrate temperatures in this way, two main difficulties appeared which I could not overcome:

The thermal conduction was highly dependent on the background pressure. With fixed temperature control circuit set on  $840\text{ }^{\circ}\text{C}$ , a change of pressure from 1 to 40 Pa lead to an increase in substrate temperature (as measured with a pyrometer) from  $790$  to  $840\text{ }^{\circ}\text{C}$ . Therefore any change in pressure (as necessary for subsequent deposition of YBCO and ZnO) necessitated new calibration of the temperature control unit, which for the ZnO deposition was very difficult due to the low deposition temperatures of  $200 - 550\text{ }^{\circ}\text{C}$  that are far outside the pyrometer's working range of  $780 - 1600\text{ }^{\circ}\text{C}$ .

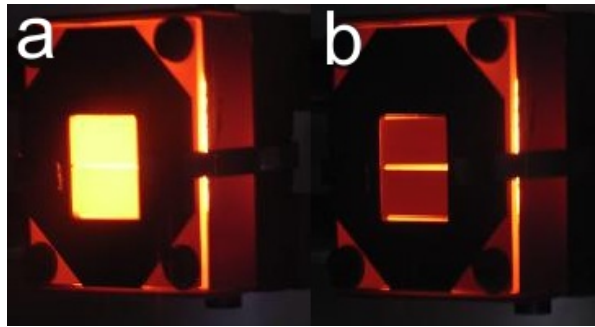


Figure 4.6: Clamping heater (thermocouple measuring  $790\text{ }^{\circ}\text{C}$  for both photos): a) before deposition, the substrate glows brightly and b) after deposition, where the film is relatively dark.

Furthermore, the deposition process changed the radiation of the substrate, while not influencing the characteristic of the thermocouple. This lead to a decrease in substrate temperature from  $\sim 800\text{ }^{\circ}\text{C}$  to less than  $760\text{ }^{\circ}\text{C}$  over the course of the deposition process (see fig. 4.6). As the pyrometer itself cannot be used for automated temperature control because it is based on the comparative capacity of the human eye, no temperature control circuit could be designed which actually monitored the substrate temperature and not the heater temperature.

For these reasons, I settled for attaching the substrates with conducting silver.

At the moment, experiments with a newly-acquired infrared-sensitive sensor to continually monitor the substrate temperature during the deposition process are conducted.

The hope is to overcome the problem of the varying thermal conduction between heater, substrate and environment.

## 4.2 Optimization of the YBCO layer

As the main goal of my thesis is the deposition of ZnO in YBCO/ZnO multilayer systems, I first had to optimize the YBCO deposition process for the fabrication of YBCO layers usable for the subsequent deposition of ZnO.

Having in mind the use of such multilayer systems for microelectronics, the attributes I tried to achieve in the films are, in descending order of importance:

- a smooth surface with no precipitates which might pierce an insulating top layer,
- very high crystallographic quality to allow epitaxial growth of subsequent layers,
- sufficient superconducting properties.

I was able to resort to the knowledge of another member of our work group who studies YBCO/STO/Au-multilayer systems to get started on the deposition of YBCO films [45]. However, the differences in the setup of our deposition chambers and the high sensitivity of the YBCO film quality on the deposition parameters forced me to fabricate extended series of YBCO samples to find the working point in which I could reliably produce smooth YBCO thin films of sufficient crystallographic quality<sup>2</sup>.

### 4.2.1 Layer thickness of YBCO films

As the profilometer method for the determination of thickness is a destructive method, it was the last measurement taken for the samples. Therefore, variation of parameters could also lead to different thicknesses which could not be compensated for.

The first samples produced at fluences around  $1.8 \text{ J cm}^{-2}$  and pressures between 20-40 Pa had 20 minutes deposition time and showed thicknesses between 400 and 900 nm.

The later samples produced at fluences around  $1 \text{ J cm}^{-2}$ , a partial oxygen pressure of 10 Pa and 7 minutes deposition time showed thicknesses between 160 and 235 nm.

### 4.2.2 Surface of YBCO films

The quality of the surface was diminished by two features: either the surface itself would have many tiny troughs, leading to a uniformly rough surface, or precipitates would form, rendering the growth of further continuous films impossible. Optical microscopy, SEM and AFM pictures of a rough surface can be seen on sample 322 in fig. 4.7, while precipitates are clearly visible on the optical and SEM pictures of sample 372 in fig. 4.8.

---

<sup>2</sup>The ZnO deposition happened in situ, therefore there was no possibility to check if the YBCO layer had the desired quality before depositing ZnO. As I was going to analyze the influence of the ZnO deposition process on the YBCO, I needed high reproducibility of the YBCO films.

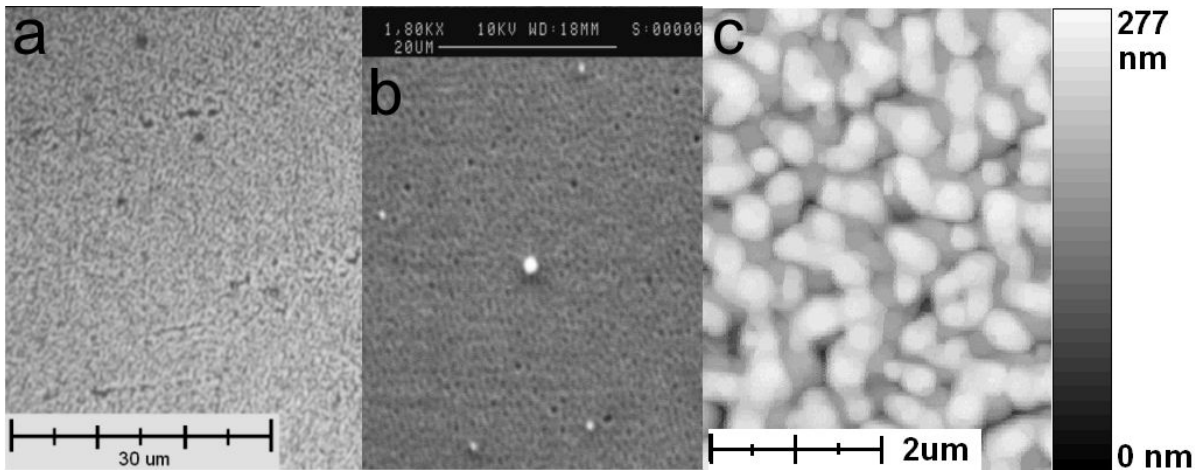


Figure 4.7: YBCO films: rough surface of sample 322: a) OM picture b) SEM picture, SE mode c) AFM scan with rms roughness of 38 nm.

As there is little contrast in the SEM picture taken in BSE mode, the precipitates probably have a stoichiometry similar to the surrounding film. In contrast, in a film in which the cooling to room temperature was performed three times slower than for the other films, precipitates formed which are of a different composition than the surrounding film (see fig. 4.9).

To show the influence of different growth temperatures, the quality of the surface, determined through an optical microscope, was rated on a scale from 0-5, 0 being very smooth and 5 very rough. As I needed to get a general impression of the influence of different parameters on the surface quality, taking AFM scans of every sample was unfeasible and the categorization by eye was sufficient to find a temperature range in which it was possible to get very smooth surfaces (see fig. 4.11): although there are some variations, only films produced at substrate temperatures between 740 °C and 775 °C show the possibility of being both very smooth and free of precipitates. In addition, a clear influence of laser fluence can also be observed in fig. 4.11, where out of six samples produced at 0.93 J cm<sup>-2</sup> only one sample is not in category 0.

To further underline the influence of laser fluence on the surface roughness, this dependence is plotted in fig. 4.12. There was always a relatively smooth and a relatively rough sample for a given fluence and it is difficult to determine a trend from the few points visible in the diagram, so I decided to also show the average of the roughnesses of all samples produced at this fluence. The data points for average roughness show a clear trend to smoother surfaces at lower laser fluences.

To further quantify these results, a few samples were analyzed by AFM measurements. The AFM measurements validated the earlier categorization: The rms roughness measured over an area of 5x5 μm<sup>2</sup> for the sample in category 3 and the one in category 2 is 50 nm and 28 nm, respectively; the four samples in category zero from which I took AFM measurements have rms roughnesses between 2.5 and 6 nm and are therefore sufficiently smooth for multi-layer fabrication.

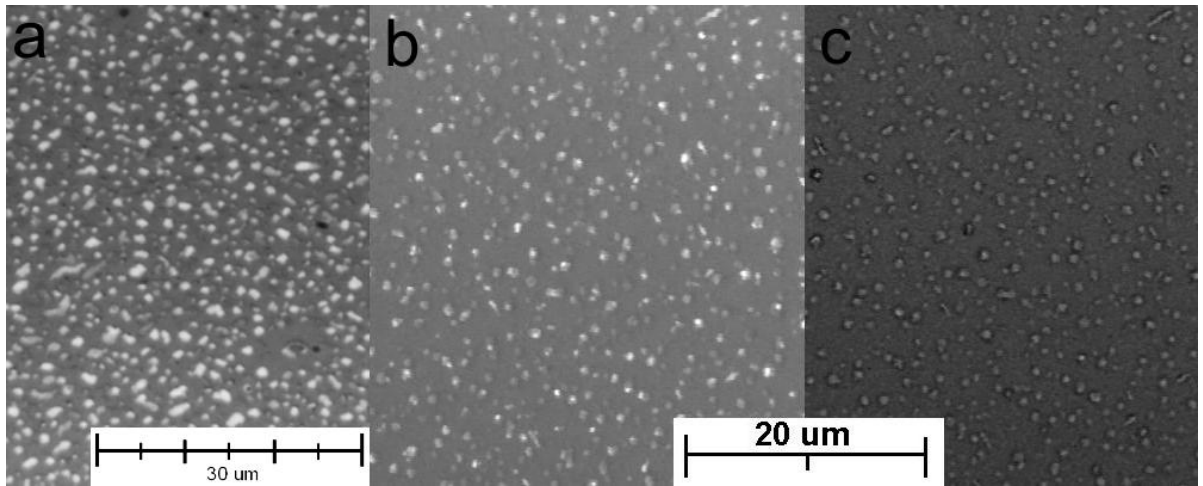


Figure 4.8: YBCO films: precipitates on sample 372: a) OM picture b) SEM picture, SE mode c) SEM picture, BSE mode: weak contrast is a sign of similar composition to the film itself.

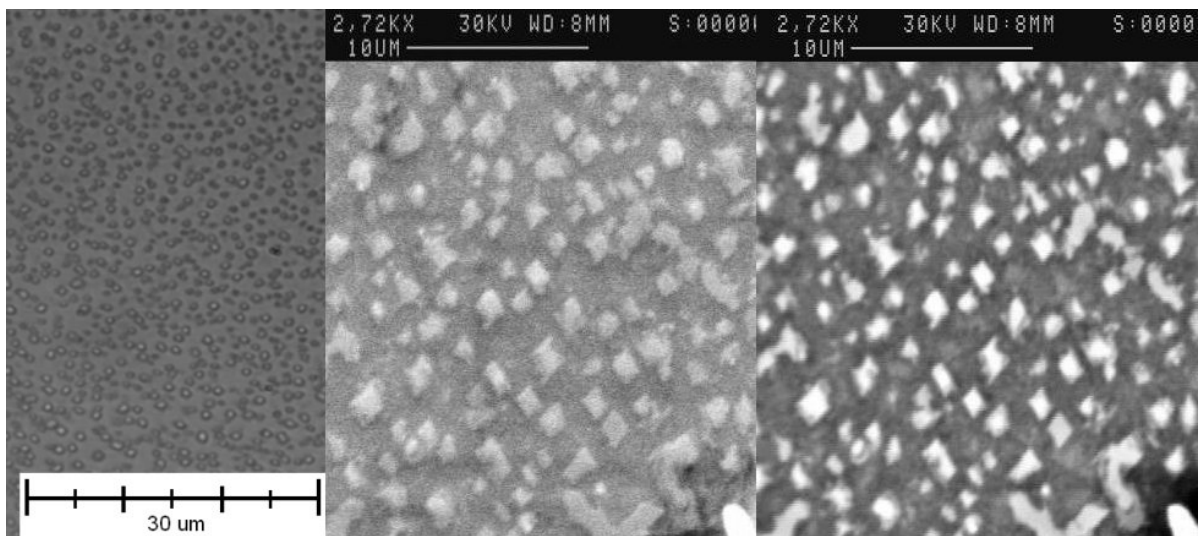


Figure 4.9: YBCO films: precipitates on surface of sample 369: a) OM picture b) SEM picture, SE mode c) SEM picture, BSE mode: strong contrast is a sign of different composition than the film.



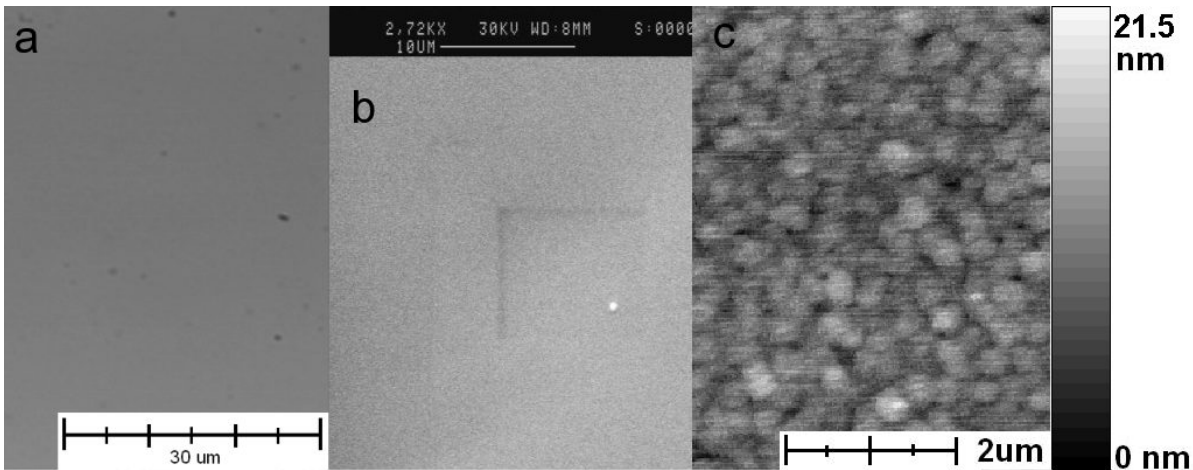


Figure 4.10: YBCO films: smooth surface of sample 366: a) OM picture b) SEM picture, SE mode c) AFM scan with rms roughness of 2.2 nm.

Optimal deposition parameters yielded surfaces as seen in fig. 4.10, where a smooth surface made up of grains with a lateral extension of  $\sim 300$  nm, but height differences of only a few nm occur. The average rms roughness is 4 nm, maximum peak-valley extension is 21 nm over the scanned  $5 \times 5 \mu\text{m}^2$ -area.

At high temperatures ( $T \sim 830^\circ\text{C}$ ), large grains with lateral dimensions of 300-400 nm form a very rough surface with an rms roughness of 50 nm and a maximal peak-valley extension of  $\sim 260$  nm (film thickness 400-800 nm). Fig. 4.7 shows a representative example, both in AFM and SEM.

This behavior seems to correspond well to the film growth theory mentioned in chapter 1.2.2. Higher temperatures lead to larger crystallites and island growth due to stronger diffusion and therefore more Oswald ripening.

In summary, very smooth films with an rms roughness of 2.5-6 nm which show neither precipitates nor holes and which have a very low droplet rate were produced at a low laser fluence of  $0.93 \text{ J cm}^{-2}$  at 10 Pa oxygen pressure in the temperature range of  $750\text{-}775^\circ\text{C}$ .

These parameters agree with the results from Veit Grosse, who is working with a different PLD setup [45]. In this PLD setup, the best YBCO films are deposited in the same temperature range at a similar laser energy, but at an oxygen partial pressure of 30 Pa. Although this pressure is much higher than my value, the plasma plumes which are very sensitive to pressure variations are very similar in size and coloring. Thus, it is likely that the deposition conditions are similar and it is only the pressure meter which monitors a different parameter due to a different PLD setup, as discussed in chapter 2.2.

### 4.2.3 Crystallinity of YBCO films

In all samples that I had produced I recorded the  $\text{YBCO}_{005}$ -peak which is proof of c-axis growth, although the intensity of the peak varied widely from 100 to 50000 counts per second (cps) for different samples. In two samples produced at low temperatures

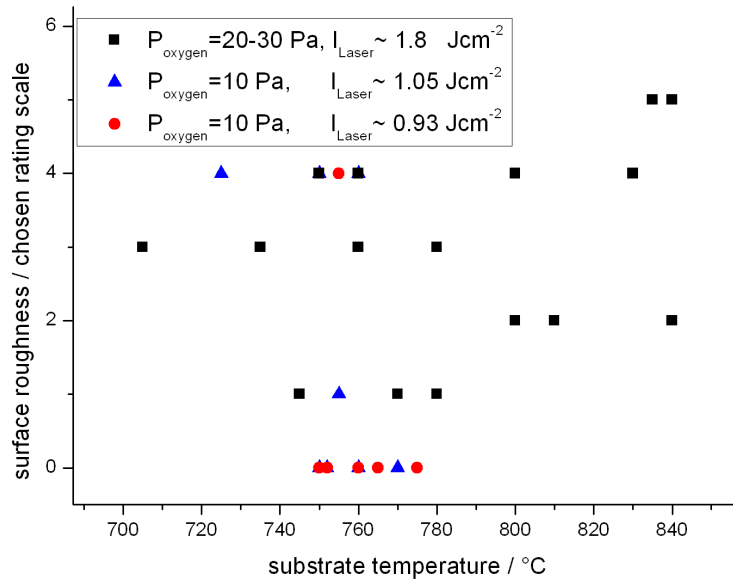


Figure 4.11: YBCO films: surface roughness vs. temperature. Smooth films were only found in the temperature range of 750-780 °C at a low laser fluence.

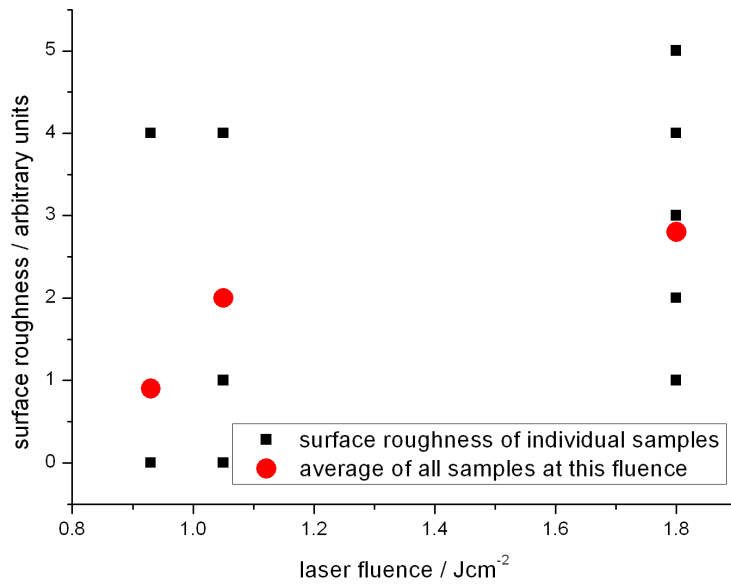


Figure 4.12: YBCO films: surface roughness vs. laser fluence. Higher fluence leads on average to a higher roughness.

( $\sim 705^\circ\text{C}$ ), I detected weak signs of a-axis growth through an asymmetric scan, as was explained in chapter 3.7.3.

### Lattice spacing

When plotting the corrected  $2\Theta$ -value of the  $\text{YBCO}_{005}$  peak for samples deposited at different temperatures and oxygen partial pressures (see fig. 4.13), two results appear: for samples produced at  $1.8\text{ J cm}^{-2}$  and 10 Pa oxygen pressure the  $2\Theta$  value increases at higher temperatures, from  $\sim 38.2^\circ$  at  $705^\circ\text{C}$  to  $\sim 38.46^\circ$  at  $840^\circ\text{C}$ , and samples produced at a lower fluence and a lower oxygen partial pressure have on average higher  $2\Theta$  values, the majority showing  $2\Theta \sim 38.45^\circ$  at  $750\text{--}770^\circ\text{C}$ .

Larger  $2\Theta$ -values result from a smaller lattice spacing:  $38.2^\circ$  equals a  $c$ -axis parameter of  $11.77\text{ \AA}$ ,  $38.46^\circ$  equals  $11.69\text{ \AA}$ . Fully oxygenated bulk YBCO has a  $c$ -axis parameter of  $\sim 11.68\text{ \AA}$ .

The change of  $c$ -axis length could be attributed to a combination of three effects. First, the film formation depends strongly on the mobility and diffusion of particles on the surface. If the substrate temperature is increased, the arriving particles have more energy to find energetically favorable positions; if the incoming particle flux is decreased through a decrease of laser fluence, the individual particles have more time to form regular unit cells. Accordingly, both changes should lead to better crystallinity, which I experimentally verified for lattice spacing and out-of-plane orientation.

Second, strain from the lattice mismatch between YBCO and STO will influence the cell parameters of the film. The thicker a film grows, the more it relaxes into its normal configuration. Therefore a sample series with strongly varying thickness with all other parameters kept unchanged and an analysis of the  $2\Theta$ -shift compared to film thickness could reveal the influence of lattice mismatch.

Finally,  $\text{YBa}_2\text{Cu}_3\text{O}_{7-x}$  cell parameters are directly influenced by the amount of oxygen ( $7-x$ ) contained. Several research groups have extracted the oxygen content from measurements of  $c$ -axis lengths. Most groups find a linear dependence in quite a large range (oxygen content 6.5-6.95), but the exact formula to calculate the oxygen content from the  $c$ -axis parameter varies from group to group, depending on different sample preparation procedures [65], [66], [67], [68]. From a graph by Ye et al. [68] in which they plot  $c$ -axis parameter over oxygen content of thin films produced by molecular beam epitaxy, I extracted the following formula used to calculate the oxygen content ( $7-x$ ):

$$7-x = (13.0476 - c) \times 5.161. \quad (4.1)$$

Although I did not independently determine the oxygen content of my samples to confirm or disprove this dependence for my samples, I observed an influence of lattice spacing on superconducting behavior, which makes such a link very probable, see chapter 4.2.5 for further details.

### Out-of-plane orientation

To evaluate the out-of-plane orientation of YBCO, the FWHM of the rocking curve of the  $\text{YBCO}_{005}$ -peak (from now on called "rocking curve FWHM") is used in almost all

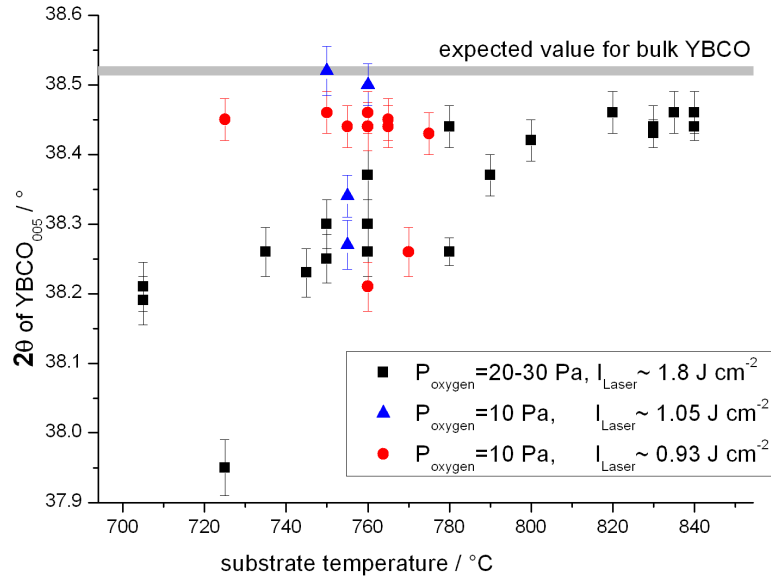


Figure 4.13: YBCO films:  $2\Theta$  vs. temperature. Higher substrate temperatures as well as a reduction of laser fluence lead to larger  $2\Theta$ -values closer to the bulk value.

scientific publications, so I will follow this convention.

To evaluate the influence of the oxygen partial pressure during deposition on the out-of-plane crystallinity of YBCO films, the rocking curve FWHM of the YBCO films deposited at pressures between 10 and 40 Pa are depicted in fig. 4.14<sup>3</sup>. When films produced at similar laser fluence and substrate temperature are compared, a lower oxygen partial pressure leads to smaller FWHM values for the rocking curves, which is equivalent to a better out-of-plane orientation.

Below 10 Pa, the coloring and size of the plasma plume undergo a drastic change, (see fig. 4.15). A test film produced at 1 Pa at  $T=850\text{ }^{\circ}\text{C}$  and  $I_{Laser}=1.8\text{ J cm}^{-2}$  had an extremely rough surface and a rocking curve FWHM of  $2^{\circ}$ , so a working pressure of 10 Pa was chosen for all further films.

The films produced at 10 Pa have rocking curves with FWHM between  $0.06^{\circ}$  and  $0.45^{\circ}$ <sup>4</sup>, depending on the other deposition parameters.

When analyzing the influence of substrate temperature on the out-of-plane orientation, the results are less clear. In fig. 4.16, the rocking curve FWHM of films deposited at different oxygen pressures and laser fluences are plotted over the substrate temperature.

The widest variation in temperature was done for films produced a 20-30 Pa and a

<sup>3</sup>Note that as these samples were produced with the heater design without conductive silver paste (see chapter 4.1.4), these values are not used for further analysis of the influence of substrate temperature in subsequent sections.

<sup>4</sup>Values below 0.13 were measured with smaller apertures, for more information see chapter 3.7.5.

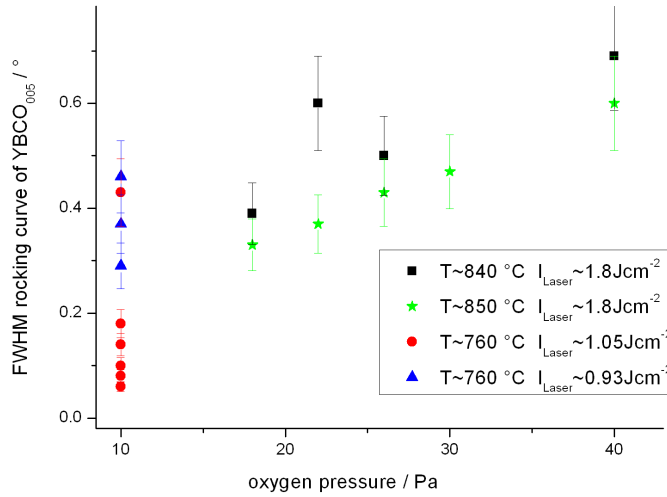


Figure 4.14: YBCO films: rocking curve vs. pressure. Higher oxygen pressure leads to worse rocking curves.

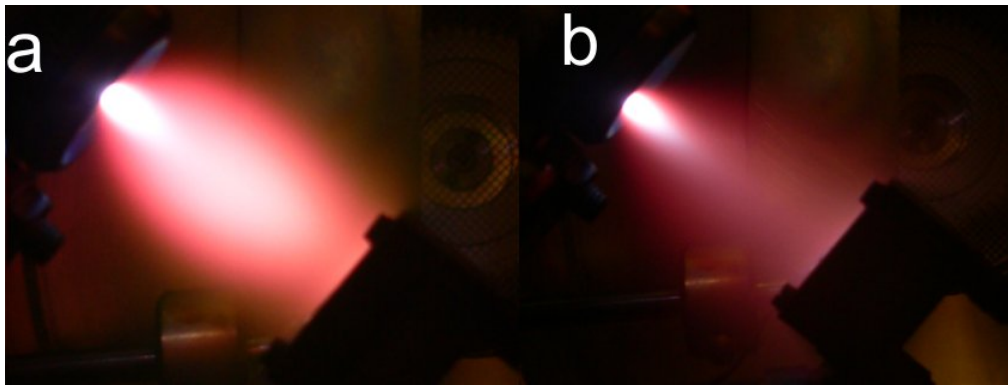


Figure 4.15: Photos of plasma plume from YBCO target: a) 10 Pa oxygen pressure b) 1 Pa oxygen pressure.

laser fluence  $I_{Laser}=1.8 \text{ J cm}^{-2}$  (black dots in fig. 4.16). At high temperatures between 830 and 840 °C, the FWHM values of the six films show only small variations between 0.1 and 0.18°, so all films produced at these parameters have a very good out-of-plane crystallinity. When decreasing the temperature, FWHM increases until reaching a maximum of ~0.47° at 790 °C. Between 700 and 790 °C, different samples show a large variation of FWHM values between 0.27° and 0.47° without a clear correlation to the temperature, although average FWHM values seem to slightly decrease with decreasing temperatures.

The samples produced at a lower oxygen pressure of 10 Pa all lie in the range of 725-775 °C, where no direct influence of the temperature on the rocking curve FWHM was observed. Instead, the laser fluence has a large impact on the out-of-plane crystallinity: at a laser fluence  $I_{Laser}=1.05 \text{ J cm}^{-2}$ , the films have rocking curve FWHM values of 0.21-

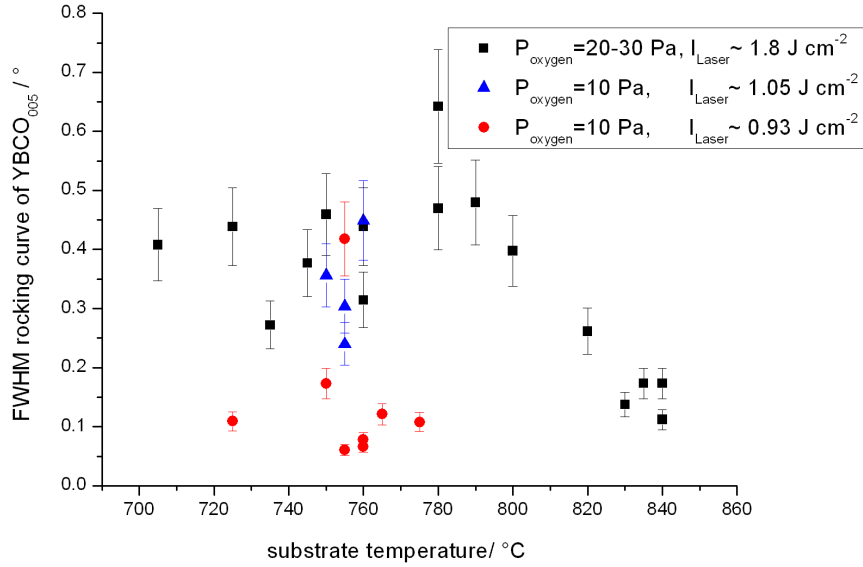


Figure 4.16: YBCO films: rocking curve vs. temperature. Average rocking curve FWHM values around  $0.4^\circ$ . FWHM values decrease strongly when increasing substrate temperatures to  $\sim 830$  K or when reducing the laser fluence at temperatures around  $760^\circ\text{C}$ .

$0.45^\circ$ . A decrease of laser fluence down to  $I_{\text{Laser}}=0.93 \text{ J cm}^{-2}$  reduces the FWHM to the range of  $0.06 - 0.41^\circ$ , with all but one sample having a FWHM of less than  $0.2^\circ$ .

In summary, the films show good crystallinity, having rocking curve FWHM values of less than  $0.5^\circ$ . Optimal conditions were found to be  $T \sim 760^\circ\text{C}$ ,  $P_{\text{oxygen}}=10 \text{ Pa}$ ,  $I_{\text{Laser}}=0.93 \text{ J cm}^{-2}$ : Most samples produced with these parameters have a  $2\Theta$ -value of  $38.45^\circ \pm 0.03^\circ$  and rocking curve FWHM values between  $0.06^\circ$  and  $0.14^\circ$  as compared to  $\sim 0.8^\circ$  before the optimization process, a sign of good epitaxial growth.

#### 4.2.4 Superconducting properties of YBCO films

The films show widely varying critical temperatures  $T_C^0$  for the transition into superconducting state between 78 and 88.5 K, as shown in fig. 4.17.

At 20-30 Pa oxygen pressure, a plateau at substrate temperatures above  $780^\circ\text{C}$  is observable with  $T_C^0$  values between 84 and 85.5 K. At lower temperatures, fluctuation between samples increases while  $T_C^0$  values decrease as low as 77.5 K.

While a reduction of oxygen partial pressure down to 10 Pa has relatively little effect, a further reduction of laser fluence down to  $0.93 \text{ J cm}^{-2}$  leads to an increase of  $T_C^0$  values up to 88.2 K. Although this transition temperature is still below the optimum transition temperature of 92 K, it is far enough away from 77 K to allow stable operation at liquid nitrogen temperature.

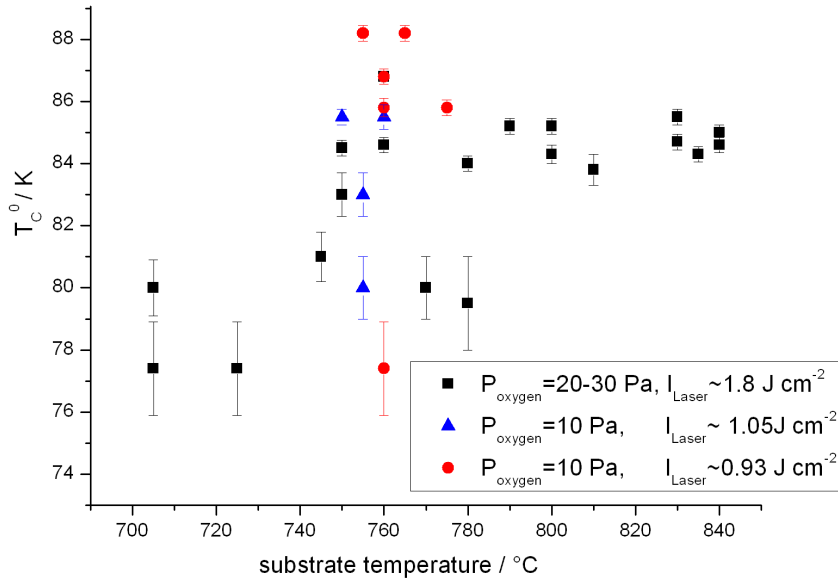


Figure 4.17: YBCO films: critical temperature vs. substrate temperature. Average  $T_C^0 \sim 84$  K, a reduction of laser fluence increases  $T_C^0$  to  $\sim 86$  K, a reduction of substrate temperature below  $750$  °C strongly reduces  $T_C^0$ .

Similar results are found for the width of the transition to superconducting state. As the substrate temperature is lowered from  $840$  to  $705$  °C,  $\Delta T_C$  rises from a reproducible  $\sim 0.9$  K to wildly fluctuating values as high as  $\sim 8$  K for samples produced at  $20$ - $30$  Pa and  $1.8$   $\text{J cm}^{-2}$  (see fig. 4.18). At a lower laser fluence of  $0.93$   $\text{J cm}^{-2}$  and an oxygen pressure of  $10$  Pa, four out of six samples showed  $\Delta T_C \leq 1$  K.

One sample was patterned as described in section 2.3 and  $j_C$  at  $77.4$  K in self-field was determined to  $j_C = (3.2 \pm 0.6) \times 10^5$   $\text{A cm}^{-2}$ .

In summary, the films show a strong dependence of superconducting properties upon the deposition parameters. At the parameters determined earlier ( $T \sim 760$  °C,  $P_{\text{oxygen}} = 10$  Pa,  $I_{\text{Laser}} = 0.93$   $\text{J cm}^{-2}$ ) moderate superconducting behavior was found: most films show  $T_C^0 \sim 87$  K,  $\Delta T_C \sim 1$  K and  $j_C$  was determined from one sample to  $j_C = (3.2 \pm 0.6) \times 10^5$   $\text{A cm}^{-2}$ .

It should be recalled that the films were optimized towards a smooth surface. The films show no precipitates and almost no droplets. Usually these objects help the film to relax strain from lattice mismatch and restore perfect stoichiometry through the expulsion of excess material. Furthermore, they act as pinning centers for flux vortices, thereby increasing  $j_C$ . Therefore, the rather moderate superconducting behavior may very well be a direct result of the film surface optimization.

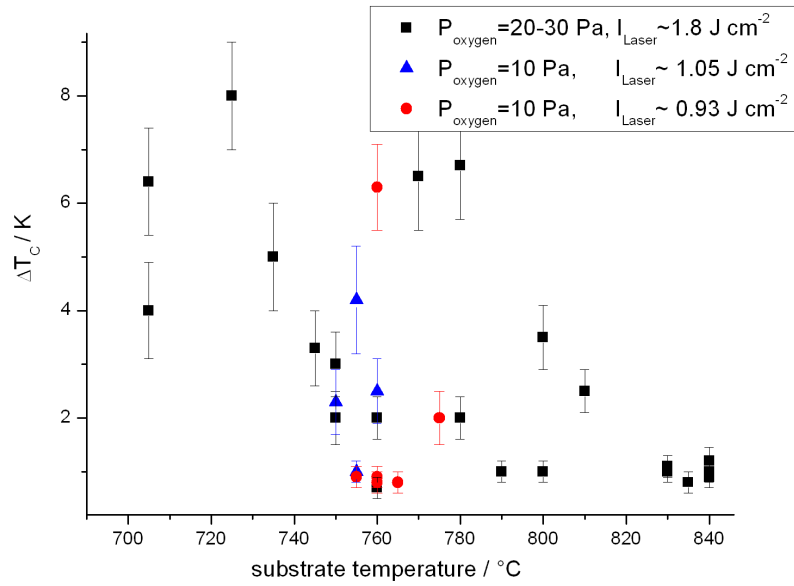


Figure 4.18: YBCO films: superconducting transition width vs. substrate temperature. As the substrate temperature increases,  $\Delta T_C$  reduces its fluctuation and decreases from  $\sim 6$  K to 1 K. A low laser fluence yields a similar low  $\Delta T_C$  already at 760 °C.

#### 4.2.5 Relation between c-axis length and superconducting properties

A comparison between  $T_C^0$  values and the c-axis length calculated from the  $2\Theta$  value can be seen in fig. 4.19. Although the individual variation is quite large, it is clear that an increase of c-axis length correlates roughly linearly to a decrease of  $T_C^0$ . A similar linear dependence of  $T_C^0$  values on c-axis length in sputtered thin films was observed by Eom et al. [69].

As mentioned in chapter 4.2.3, a linear dependence of oxygen content on c-axis length was observed by several research groups. I calculated the oxygen content of my films with equation (4.1) for thin YBCO films deposited by molecular beam epitaxy, and plotted the  $T_C^0$  values over the calculated oxygen content in fig. 4.20. The trend of increasing  $T_C^0$  with increasing oxygen content is very well observed.

Several groups report that when studying the relation between  $T_C^0$  and oxygen content of YBCO thin films, the plateaus usually observed for bulk material become less prominent, giving way to a roughly linear dependence [68],[69]. When comparing their results with my values, something seems amiss. The calculation yields high oxygen concentrations of  $> 7$  for some samples, while for other samples with an oxygen content of  $\sim 6.6$  I should hardly be able to measure  $T_C^0$  above liquid nitrogen temperatures at all.

This gives rise to the assumption that the formula used to calculate oxygen concentra-



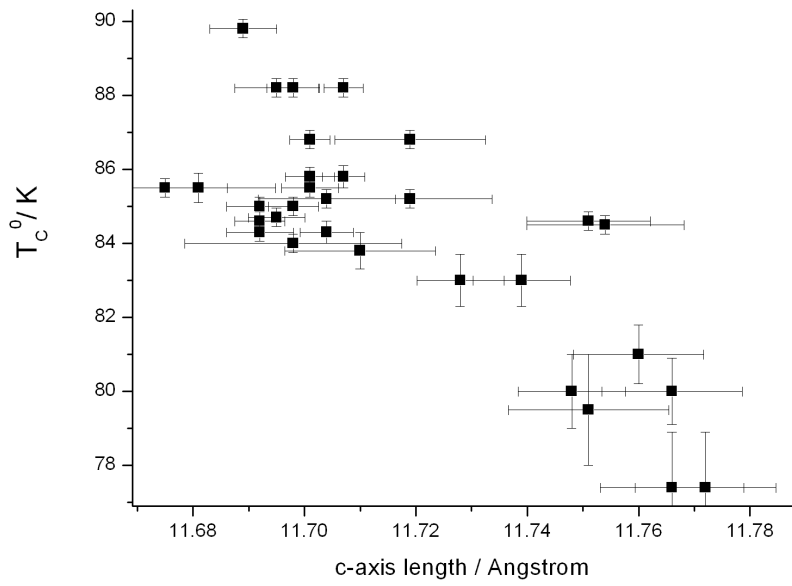


Figure 4.19: YBCO films: critical temperature vs. c-axis length.  $T_C^0$  decreases roughly linearly with c-axis length.

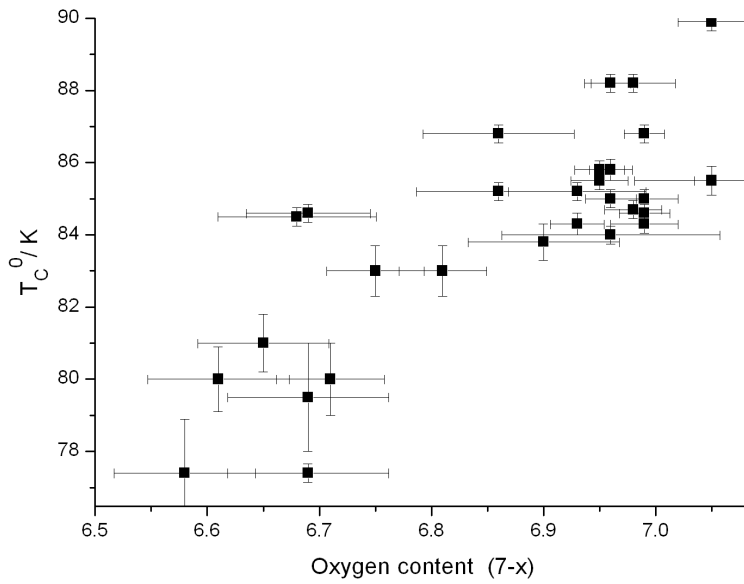


Figure 4.20: YBCO films: critical temperature vs. oxygen content calculated from c-axis length. A roughly linear dependence is observable, but the absolute values do not fit literature values.

tion is not appropriate for my samples. A spread of oxygen content of 0.47 (from 6.58 to 7.05) should yield a larger spread of  $T_C^0$  values than the one observed. For a new mathematical formulation of the relation between c-axis length and oxygen content for my samples, it would be necessary to perform other measurements like Raman spectroscopy [67], [70] or IR reflectance and transmittance measurements [71] to directly determine the oxygen concentration of a few chosen samples.

In summary, a roughly linear dependence of  $T_C^0$  on c-axis length was found. The exact relations between c-axis length, oxygen content and  $T_C^0$  could not be reproduced with formulas from literature. The scope of this thesis did not allow the collection of a sufficient amount of data to form the basis for a new mathematical description.

## 4.3 Analysis of the ZnO layer

After the deposition conditions for the YBCO layer were optimized, ZnO films were deposited in situ on the YBCO film for 3, 7 and 20 minutes at 1 or 10 Pa oxygen pressures, at temperatures between 200 and 500 °C and at a fixed laser fluence of  $2.0 \text{ J cm}^{-25}$ .

### 4.3.1 General remarks

Film thicknesses as measured with RBS were 920-1020 nm for 20 min deposition time, 220-370 nm for 7 min deposition time and 120-180 nm for 3 min deposition time.

For films deposited at 1 Pa oxygen pressure, the plasma plume was much smaller and more focused than the plume at 10 Pa (see fig. 4.21). Most ZnO films deposited at 1 Pa show a lateral inhomogeneity which probably can be attributed to this focused plasma plume. The composition and velocity of the particle flux depends strongly on whether the inner part or the bright periphery of the plume touches the sample. The broad plume at 10 Pa has a much larger center which almost always covers the whole

---

<sup>5</sup>The high laser fluence was chosen because most other research groups have produced good results with similar fluences.



Figure 4.21: Photos of plasma plume from ZnO: a) 1 Pa oxygen pressure b) 10 Pa oxygen pressure.

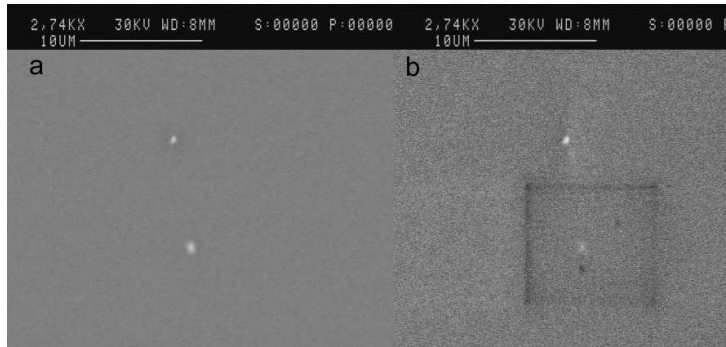


Figure 4.22: ZnO films: surface of sample 362: a) SEM picture, BSE mode b) SEM picture, SE mode.

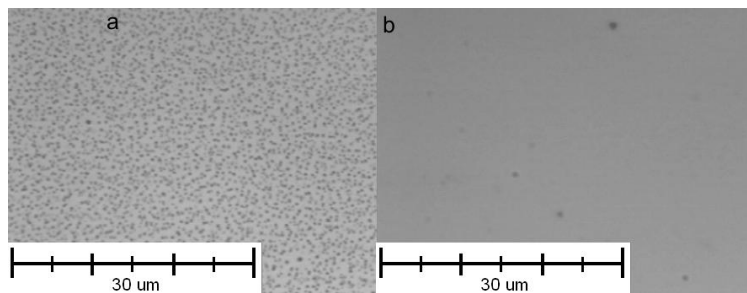


Figure 4.23: ZnO films: surface of sample 380: a) OM picture, upper part, lots of precipitates b) OM picture, middle part, smooth surface.

5x10 mm<sup>2</sup> substrate, so the exact positioning of substrate to target is not as critical as for the 1 Pa plume.

### 4.3.2 Surface of the ZnO layer

The ZnO surface of most samples is relatively smooth, with an rms roughness of about 6 nm<sup>6</sup>. From SEM pictures with backscattered electrons it can be deduced that the surface composition is uniform (see fig. 4.22).

Droplet densities are comparable to those measured for the YBCO base layer, so the ZnO deposition process seems to add almost no new droplets.

The upper part (when glued to the heater) of the surface of some samples shows lots of precipitates (see fig. 4.23). As the middle part was always free of precipitates, these areas were used for AFM analysis of the surface. AFM pictures of chosen samples can be seen in fig. 4.25.

Relatively little influence of substrate temperature on the surface roughness could be detected. Except for two samples with deposition times of 20 min and substrate temperatures above 350 °C with rms roughnesses of 29 and 32 nm, all samples show an rms roughness between 4 and 8 nm (see fig. 4.24).

<sup>6</sup>The base YBCO layers have a surface roughness of 2.5-6 nm.

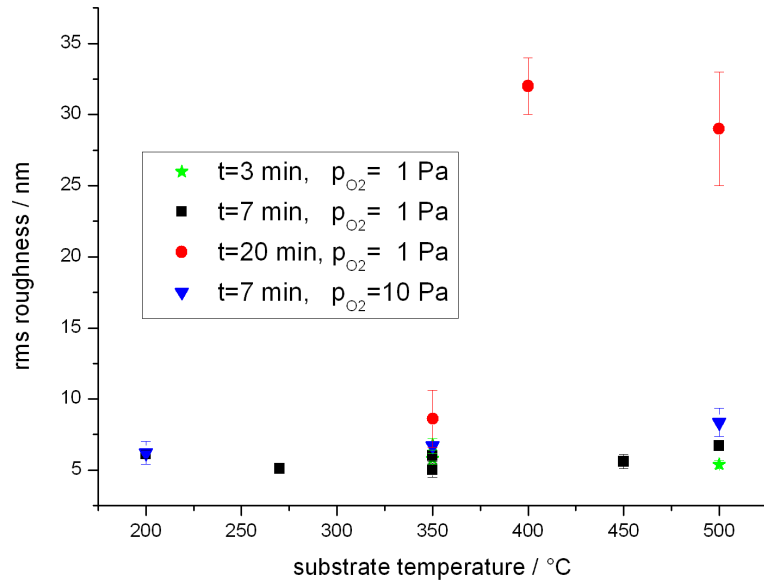


Figure 4.24: ZnO films: surface roughness vs. substrate temperature. Most films are smooth, only films deposited for 20 min at high temperatures show a strongly increased roughness.

However, the surface morphology changes, as can be seen in fig.4.25. Compared to the samples produced at  $T \leq 350^\circ\text{C}$  and 1 Pa which show crystallites with a size of 40-70 nm which sometimes cluster together to  $\sim 200$  nm large agglomerations, the samples produced at a higher oxygen pressure of 10 Pa show larger crystallites of 100-150 nm which seem to be spread more evenly. This agrees well with findings by other groups: below  $\sim 15$  Pa, increasing oxygen pressure increases crystallite size [54], [51].

At high temperatures (400-500 °C), the sample deposited at 1 Pa for 3 min shows crystallites with a lateral size of 50-130 nm. Upon increasing the deposition time, the small crystallites seem to coalesce and continue to grow into very large clusters of  $\sim 300$  nm size with little internal structure visible.

In summary, very smooth films were deposited. Except for the films deposited above 350 °C for 20 min, all films showed smooth surfaces with rms roughness of 4-8 nm. Given that the YBCO films used as base layers had themselves an rms roughness of 2.5-6 nm, these values are excellent, and even in comparison to literature values of films deposited on lattice-matched polished substrates, they are still good.

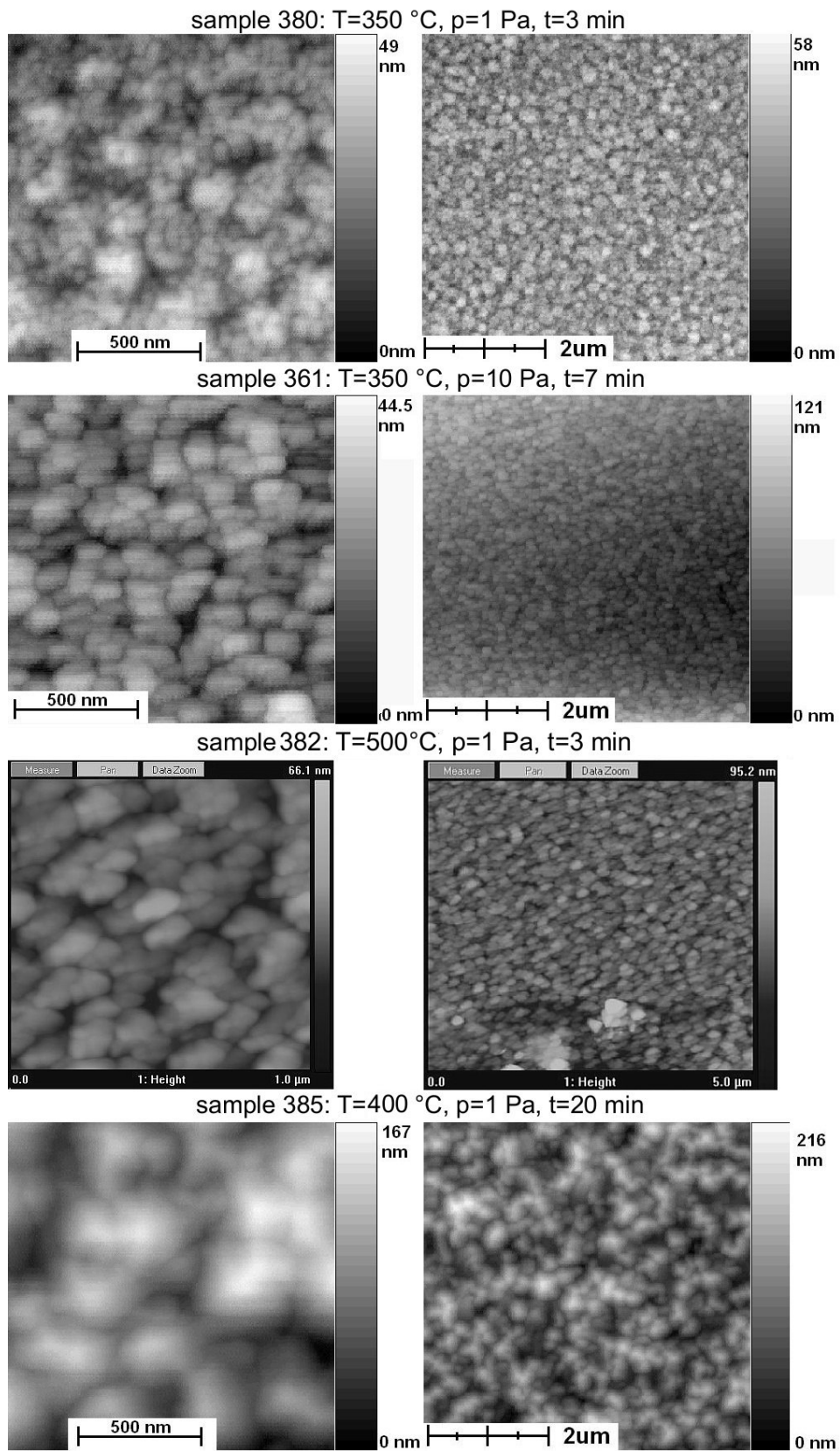


Figure 4.25: ZnO films: AFM pictures of chosen sample.

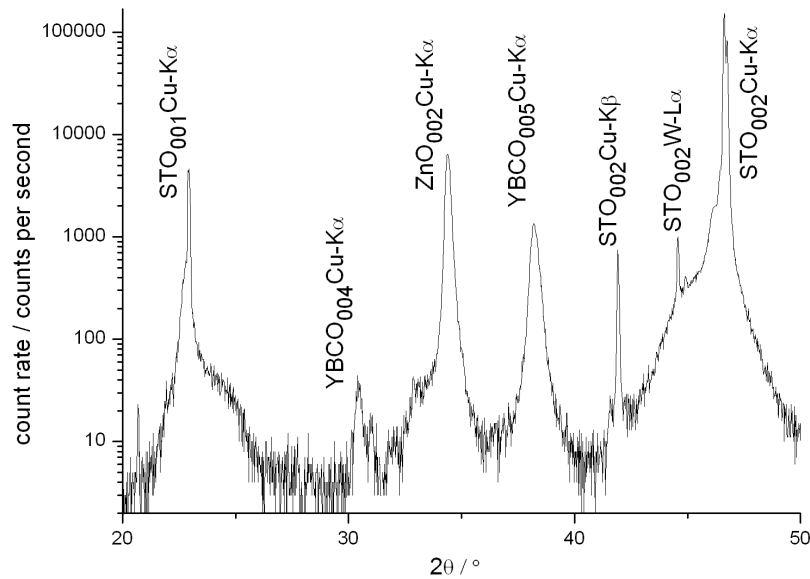


Figure 4.26: XRD chart:  $\omega$ - $2\theta$ -scan of sample with ZnO on YBCO on STO.

### 4.3.3 Crystallinity of the ZnO layer

In all samples I detected the  $\text{ZnO}_{002}$ -peak at  $2\theta \sim 34.3^\circ$  which is proof of  $c$ -axis growth, although the intensity of the peak varied widely between samples, from 50 to 30000 counts per second with the same measurement setup. For a sample XRD chart, see fig. 4.26.

In a few samples I also found some  $a$ -axis growth as there was a peak at  $2\theta \sim 31.6^\circ$  which coincides well with the  $\text{ZnO}_{100}$ -peak at  $31.8^\circ$ . This peak was always smaller than the  $c$ -axis peak by a factor of 3-10.

#### Lattice spacing and crystallite size

When plotting the corrected  $2\theta$ -value of the  $\text{ZnO}_{002}$  peak for samples deposited at 1 Pa oxygen pressure at different temperatures (see fig. 4.27), no clear relation is apparent, although a general trend is that higher temperatures lead to increasing  $2\theta$  values. One sample at  $200^\circ\text{C}$  showed  $2\theta \sim 33.7^\circ$  while at  $500^\circ\text{C}$  several samples had  $2\theta \sim 34.3^\circ$ .

The samples produced at a higher oxygen partial pressure of 10 Pa show larger  $2\theta$  values with only a tiny increase from  $34.28^\circ$  at  $200^\circ\text{C}$  to  $34.4^\circ$  at  $500^\circ\text{C}$ .

These  $2\theta$ -values result from the following lattice spacings:  $33.7^\circ$  equals a  $c$ -axis parameter of  $5.31 \text{ \AA}$ ,  $34.4^\circ$  equals  $5.21 \text{ \AA}$ . As bulk ZnO has a  $c$ -axis parameter of  $5.204 \text{ \AA}$ , the ZnO films are stretched in  $c$ -axis direction, but higher temperatures and higher oxygen pressures lead to a decrease of  $c$ -axis length close to the bulk value.

Ohshima et al. [28] observed similar behavior for the deposition of ZnO on Si and corning glass at comparable temperatures and pressures, although their  $2\theta$  values vary

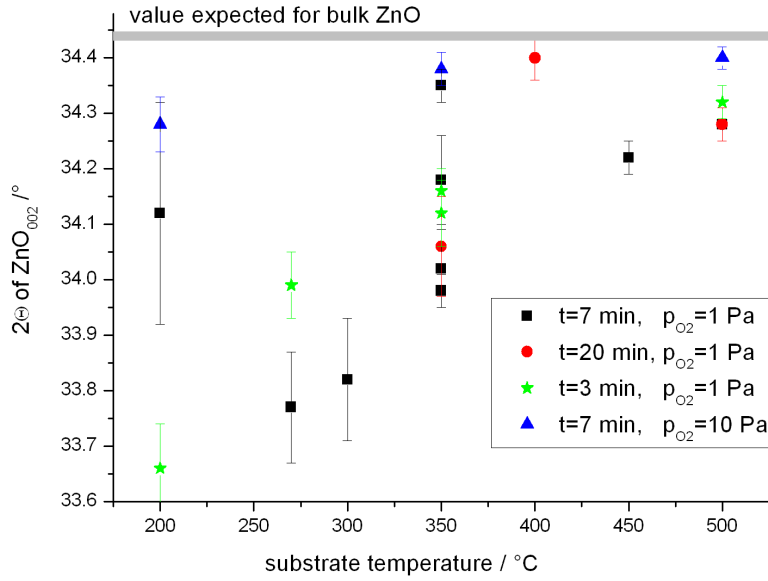


Figure 4.27: ZnO films:  $2\Theta$  of  $\text{ZnO}_{001}$  vs. substrate temperature. Increase of substrate temperature as well as increase of oxygen pressure lead to higher  $2\Theta$  values (closer to the bulk value).

between  $34.34^\circ$  and  $34.55^\circ$ . This difference in absolute length might be due to the different substrate, although it seems improbable that the ZnO layer would not relax to normal lattice parameters in a 150-350 nm thick film. Ohshima et al. try to explain the change in c-axis with either a difference in oxygen content or a difference in thermal expansion coefficient between film and substrate, as they use  $\text{SiO}_2$  with an  $\alpha_{ab}$  half that of ZnO. As the films deposited on YBCO show the same behavior of decreased c-axis length for higher substrate temperatures despite the  $\alpha_{ab}$  of YBCO and STO being twice that of ZnO, the influence of the thermal expansion coefficient seems minimal.

Using the Debye-Scherrer equation (see eq. (3.2)), I calculated the ZnO crystallite sizes from the  $\omega-2\Theta$ -scan FWHM values corrected for diffractometer broadening according to eq. (3.3) and plotted them in fig. 4.28. Note that although I present error bars calculated from the FWHM of the  $\omega-2\Theta$ -scan, there may be a much larger error due to unknown geometry factors<sup>7</sup>, therefore the sizes should not be taken as exact values but rather show trends for changing parameters.

Upon increasing the pressure from 1 to 10 Pa, the films deposited for 7 min show twice or three times the crystallite size. Furthermore, a steady increase of crystallite size for increasing substrate temperature is visible for all deposition parameters. A similar increase of crystallite size with temperature was also found by Park et al. [73].

In contrast to the surface analysis by AFM, which showed that a longer deposition

<sup>7</sup>For further information, see chapter 3.7.2 or a more detailed discussion in [72].

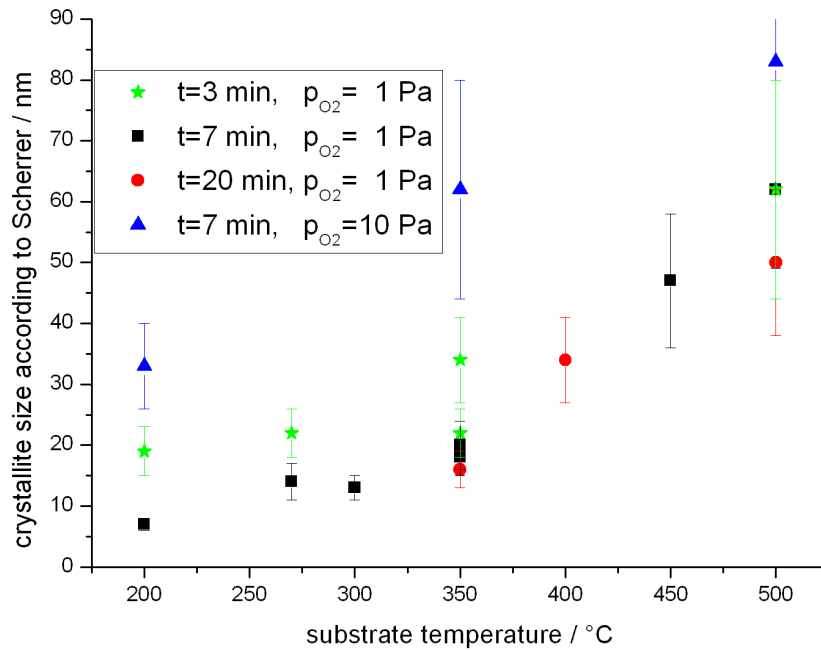


Figure 4.28: ZnO films: crystallite size vs. substrate temperature. Films deposited at 10 Pa show much larger crystallites, also crystallite size increases with substrate temperature.

time leads to larger grain sizes, the crystallite size as determined through XRD analysis seems to stay the same or even slightly decrease upon increase of deposition time.

### Crystal orientation

To determine the influence of substrate temperature, deposition time and oxygen partial pressure on the out-of-plane orientation, the rocking curves of the  $\text{ZnO}_{002}$ -peak were measured and their FWHM values plotted in fig. 4.29.

The out-of-plane orientation of the ZnO layer depends strongly on the substrate temperature: for all deposition conditions, the rocking curve FWHM drops continually as the substrate temperature is raised from 200 to 500 °C. At 500 °C, a rocking curve FWHM of  $0.90^\circ \pm 0.2^\circ$  is reached for all deposition parameters.

The other deposition parameters also influence the crystallinity. Both shorter deposition times as well as the increase of oxygen partial pressure from 1 to 10 Pa generally lead to a lower rocking curve FWHM value.

No offset between the YBCO *c*-axis and the ZnO *c*-axis could be detected. Within the measurement accuracy of  $0.2^\circ$ - $0.5^\circ$ , they were parallel to each other.

To determine the in-plane orientation of the ZnO sample I first chose the  $\text{ZnO}_{101}$ -peak at  $2\theta \sim 36.3^\circ$  and  $\chi \sim 61.6^\circ$ , calculated from eq. (1.4). However, I noticed that YBCO



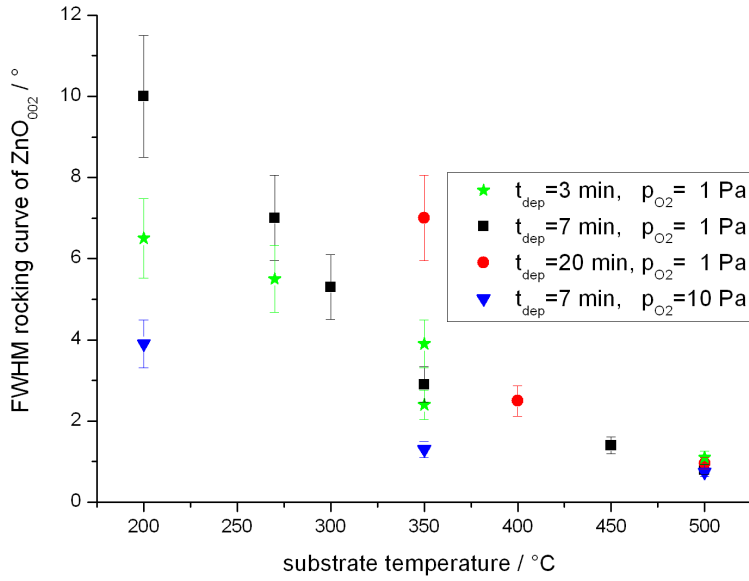


Figure 4.29: ZnO films: Rocking curve vs. substrate temperature. A roughly linear decrease of rocking curve FWHM with increasing substrate temperature is observed. Increasing the oxygen pressure also leads to better out-of-plane orientation.

has a peak at similar angles ( $2\Theta \sim 36.3^\circ$  and  $\chi \sim 64.9^\circ$ ), the tail of which sometimes interferes with the measurement of the ZnO peaks due to the large apertures I had to use. I therefore shifted to the  $\text{ZnO}_{103}$ -peak at  $2\Theta \sim 62.9^\circ$  and  $\chi \sim 31.6^\circ$  which has only half the intensity of the  $\text{ZnO}_{101}$ -peak.

A  $\phi$ -scan at these angles showed a 12-fold symmetry (see fig. 4.30), as was expected: when positioning a hexagon on a square, a rotation by  $30^\circ$  leaves the situation unchanged as can be seen in fig. 4.32. The  $\text{ZnO}_{103}$  peaks are shifted by  $15^\circ$  in relation to the  $\text{YBCO}_{102}$  peaks.

I determined the FWHM values of the  $\phi$ -scan and plotted them over the rocking curve FWHM values in fig. 4.31. A linear dependence is clearly visible, so at least for the growth on YBCO, the in-plane-orientation of ZnO seems directly connected to the out-of-plane orientation. Therefore it should suffice to determine the rocking curve FWHM in further parameter variations of ZnO films.

Fouchet et al. [51] find a similar strong in-plane orientation when depositing ZnO on (001)- $\text{Al}_2\text{O}_3$ , while other groups like Zerdali et al. [57] or Wang et al. [74] find no in-plane orientation at all when depositing ZnO on amorphous  $\text{SiO}_2$ . The YBCO sublayer seems to improve the in-plane orientation of the ZnO film compared to a deposition on amorphous material. This is surprising, as an optical analysis of the positioning of the hexagonal ZnO structure on the orthorhombic YBCO structure does not immediately reveal that a  $15^\circ$  offset is energetically favorable to other positions (see fig. 4.32).

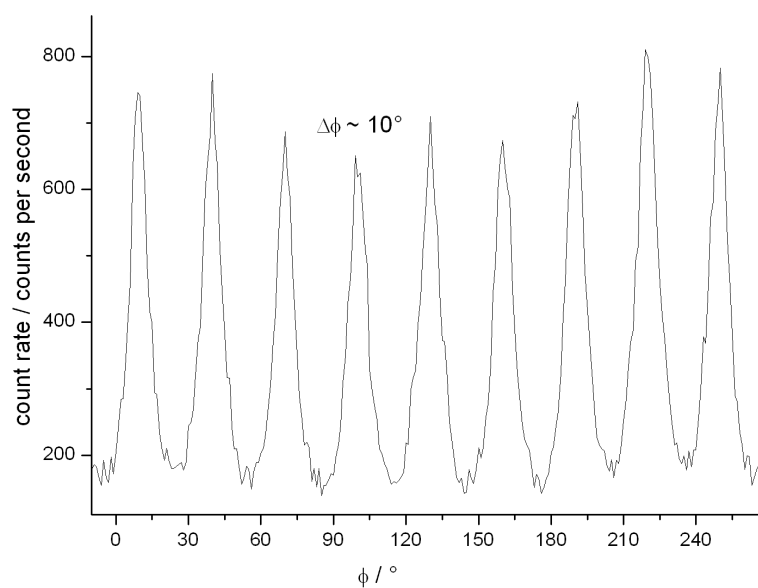


Figure 4.30: ZnO films:  $\phi$ -scan of sample 385. A twelve-fold symmetry is observed, with  $\phi$ -scan FWHM of about  $10^\circ$ .

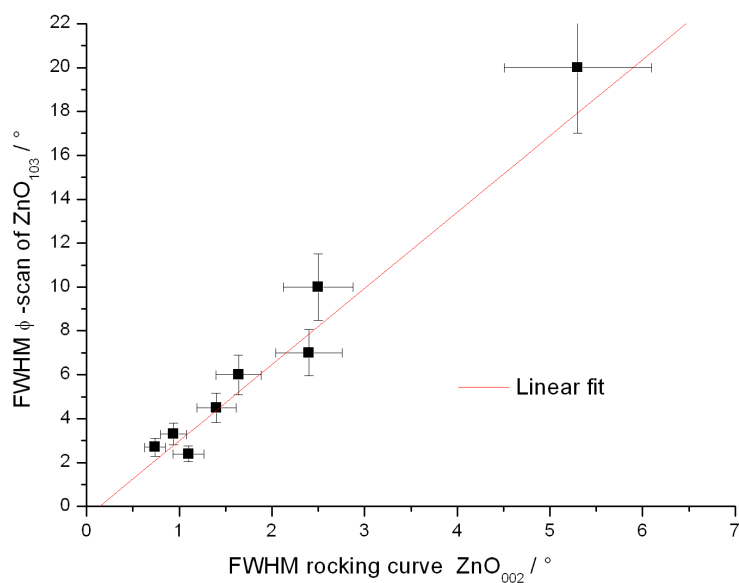


Figure 4.31: ZnO films:  $\phi$ -scan vs rocking curve. The in-plane orientation shows a linear dependence on out-of-plane orientation.

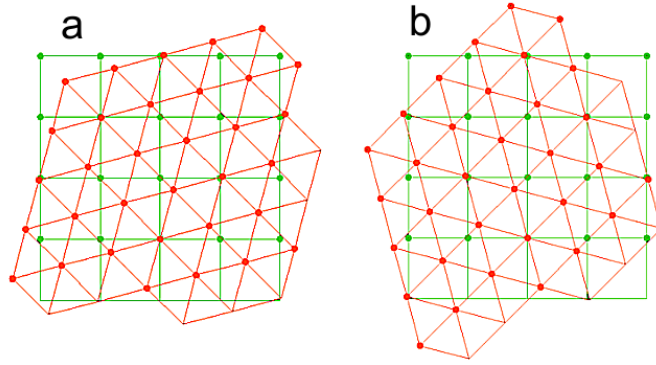


Figure 4.32: Observed positioning of the hexagonal ZnO lattice on the orthorhombic YBCO lattice: a) 15° offset between ZnO and YBCO b) rotating the ZnO by 30° leaves the situation unchanged, therefore a 12-fold symmetry is observed in the  $\phi$ -scan.

#### 4.3.4 YBCO degradation due to ZnO deposition

To determine whether the YBCO layer is degraded by the ZnO deposition, the parameter easiest to measure is the plane spacing accessible by XRD. The ZnO layer is thin enough to still allow exact determination of the YBCO<sub>005</sub>-peak (1-20 kcps) and the plane spacing will definitely change if either the YBCO film becomes oxygen-deficient or zinc diffuses into the YBCO lattice.

The measured  $2\Theta$ -values are plotted over the substrate temperature in fig. 4.33 for all samples.

For high oxygen pressures or short deposition times the  $2\Theta$ -value shifts only slightly to lower values, so the YBCO apparently does not change significantly.

The minimal shift of  $-0.05^\circ$  observed in the two samples deposited for 20 min at 350 and 400 °C is difficult to explain. It might be argued that already a thin layer of ZnO seals the YBCO film and makes further oxygen loss difficult, so that the main oxygen loss happens during the heating to deposition temperature. This would explain that films deposited for 20 min do not show a much stronger reduction of  $2\Theta$ . However, the samples produced at 7 min and 1 Pa show a larger shift of up to  $-0.2^\circ$  at temperatures below 400 °C, increasing to  $-0.4^\circ$  at 450 °C. Therefore the idea of a sealing ZnO-layer is rejected, and further analysis would be necessary to find an explanation.

For 7 and 20 min deposition time at an oxygen partial pressure of 1 Pa, the YBCO-peak shifts strongly at 500 °C (from  $\sim 38.45^\circ$  to  $\sim 37.8^\circ$ ), so the YBCO-film loses much of its oxygen and maybe some other diffusive or phase-changing process takes place.

In future experiments, it would be interesting to measure the superconducting properties of the YBCO layer underneath the ZnO. While it seems very probable that the layers with strongly reduced  $2\Theta$  values will have very poor superconducting properties, it is difficult to make assumptions about the layers with unchanged  $2\Theta$ . The superconductivity in YBCO is quite sensitive to even minor contamination with certain materials. Even a 2%-doping with Zn can strongly reduce the  $T_C^0$  by 5-30 K [75], [76].

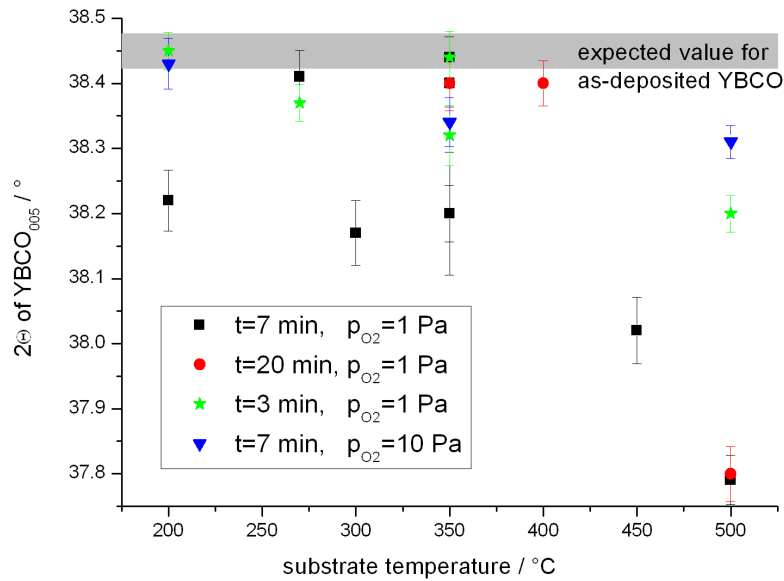


Figure 4.33: ZnO films: YBCO  $2\theta$  vs. substrate temperature. Films deposited at low oxygen pressures, extended time and high temperatures show medium to severe degradation.

### 4.3.5 Optimal deposition conditions

From the above-mentioned individual measurements it can be concluded that out of the parameters I tested, the films deposited for 7 minutes at 350 °C and an oxygen partial pressure of 10 Pa show the best combination of a smooth surface (rms roughness  $\sim 6$  nm), good crystallinity (rocking curve FWHM  $\sim 1.3^\circ$ ) and a low degradation of the underlying YBCO layer ( $2\theta$  value  $\sim 38.35^\circ$ ).

### 4.3.6 Comparison of different substrates

Two films were deposited on STO without prior deposition of YBCO to check if the deposition on a thin YBCO film produces a different ZnO layer than a deposition on a single-crystal STO substrate.

Deposition parameters were chosen as follows:  $T_{\text{substrate}} = 350^\circ\text{C}$ ,  $p_{\text{oxygen}} = 10$  Pa,  $t_{\text{deposition}} = 7$  min. The resulting films had a slightly better crystallinity than the film deposited on YBCO (rocking curve FWHM  $0.94^\circ$  and  $0.7^\circ$  instead of  $1.3^\circ$  for films deposited on YBCO) and showed a smooth surface (rms roughness = 1.7 nm over a  $5 \times 5 \mu\text{m}$  area).

# 5 Conclusion and outlook

In this thesis I discussed the fabrication and analysis of ZnO/YBCO-multilayers on STO substrates via pulsed laser deposition.

To begin with, the PLD setup was analyzed and some parts were changed. Experiments with a clamping substrate holder to simplify substrate exchange and to overcome contamination of films by conductive silver paste did not produce the expected results. The thermal conduction between heater and substrate was suboptimal, it depended strongly on the oxygen partial pressure, making a recalibration necessary. Furthermore, the thermal conduction was so weak that the change of emission of the substrate over the course of the deposition process lead to a change in substrate temperature. Therefore, the clamping heater design was abandoned in favor of the well-tested conductive silver paste contact heater.<sup>1</sup>

In contrast, a different change of the setup proved very successful: the combination of sanding the target before each deposition, decreasing the laser fluence at the target and slightly defocusing the laser spot to create a somewhat larger laser focus with sharp edges resulted in a huge decrease of droplet density from  $\sim 1 \times 10^6 \text{ cm}^{-2}$  down to  $5 \times 10^4 \text{ cm}^{-2}$ . This density is low enough to make the films very suitable for multilayer devices.

For the deposition and analysis of ZnO on YBCO, it was first necessary to analyze the YBCO film growth and to find parameters for the reproducible deposition of YBCO films. The parameters were optimized towards a later use as base layer for ZnO films. Thus, surface smoothness and crystallinity had priority over superconducting properties.

This goal was achieved: 200 nm thin, very smooth films with an rms roughness of 2.5-6 nm, showing neither precipitates nor holes and having a very low droplet density, were produced at a low laser fluence of  $0.93 \text{ J cm}^{-2}$  at 10 Pa oxygen pressure in the temperature range of 750-775 °C. All films showed c-axis growth with good crystallinity, having rocking curve FWHM values of less than  $0.5^\circ$ . Optimal conditions were found to be  $T \sim 760^\circ \text{C}$ ,  $p_{\text{oxygen}} = 10 \text{ Pa}$ ,  $I_{\text{Laser}} = 0.93 \text{ J cm}^{-2}$ : Most samples produced with these parameters had rocking curve FWHM values between  $0.06^\circ$  and  $0.14^\circ$  combined with a  $2\Theta$ -value of  $38.45^\circ \pm 0.03^\circ$ .

The films showed a strong dependence of superconducting properties upon the deposition parameters. At the parameters determined earlier, moderate superconducting behavior was found: most films showed  $T_C^0 \sim 87 \text{ K}$ ,  $\Delta T_C \sim 1 \text{ K}$ , and  $j_C$  was determined from one sample to  $j_C = (3.2 \pm 0.6) \times 10^5 \text{ A cm}^{-2}$ . The smooth surface probably has a negative influence on superconducting behavior, as droplets and precipitates usually

---

<sup>1</sup>Should an automated temperature control loop for the substrate surface become available, e.g., based on an IR temperature sensor, the clamping heater might yet prove useful.

allow film relaxation and act as pinning centers.

A comparison of c-axis parameter and  $T_C^0$  yielded a roughly linear dependence. However, none of the widely varying literature values for the calculation of oxygen content from c-axis length and subsequent comparisons to  $T_C^0$  fit well to my values. It would be interesting to use other methods of oxygen determination like Raman spectroscopy or IR reflectance and transmittance measurements to test if a direct linear dependence of oxygen content on c-axis length can be found for the films produced for this thesis.

On YBCO films produced with these optimal parameters I deposited 140-1000 nm thick ZnO films at 1 and 10 Pa and temperatures between 200 and 500 °C. Except for the films deposited above 350 °C for 20 min, all films showed smooth surfaces with rms roughness of 4-8 nm measured over an area of  $5 \times 5 \mu\text{m}^2$ . Given that the YBCO films used as bases layers had themselves an rms roughness of 2.5-6 nm, these values are excellent, and even in comparison to literature values of films deposited on lattice-matched polished substrates, they are still good. A film that I directly deposited on STO substrate had an rms roughness of 1.5 nm.

All films showed c-axis orientation, a few samples also showed weak a-axis growth. Higher deposition temperature lead to a shorter c-axis parameter as well as better rocking curves. The best rocking curve FWHM of  $0.74^\circ$  was reached at 500 °C with 10 Pa oxygen pressure. For the ZnO films analyzed, the in-plane orientation showed a linear dependence on out-of-plane orientation, in contrast to the results of some other groups who see very high out-of-plane orientation but no in-plane-orientation at all. This high degree of epitaxy is impressive, given that the orthorhombic lattice of YBCO and the hexagonal lattice of ZnO do not match at all.

Finally, the degradation of the underlying YBCO film through the ZnO deposition process was analyzed by XRD. For high temperatures and long deposition times, a strong increase of c-axis length to  $11.89 \text{ \AA}$  was observed. Lower temperatures, shorter deposition times and higher oxygen pressures lead to only slight increases of c-axis length ( $\sim 11.71 \text{ \AA}$ ) compared to the values measured for as-deposited films ( $11.69 \text{ \AA}$ ).

The best mix of very smooth surface (rms roughness 6.7 nm measured over an area of  $5 \times 5 \mu\text{m}^2$ ), high crystallinity (rocking curve FWHM  $1.3^\circ$ ) and low YBCO degradation (c-axis parameter  $11.73 \text{ \AA}$ ) was observed for the film deposited for 7 min at 10 Pa and a substrate temperature of 350 °C.

In summary, this thesis analyzes the first pulsed laser deposition of ZnO thin films on YBCO films on STO substrates. Despite the difference in symmetry between the ZnO and YBCO lattice, epitaxial growth of very smooth ZnO layers on YBCO was achieved.

Now that a parameter field is identified in which ZnO on YBCO films with high quality can be produced, it will be very interesting to measure electrical and optical properties.

First, the ZnO layers should be characterized. Hall measurements could be used to determine the charge carrier density in ZnO, although the YBCO film would probably strongly interfere. One resort could be Hall measurements of ZnO films deposited on STO with the same deposition parameters as the films deposited on YBCO. Although there will surely be some variation due to the change of base layer, it should at least be

possible to infer the order of magnitude of charge carrier density and resistivity of the ZnO-on-YBCO films.

Detailed investigations of the interfaces and the conducting mechanisms should follow. Complex film patterning could be used to fabricate capacitive YBCO/ZnO/Au structures, allowing the measurement of I-V characteristics from which the resistivity and the dielectric constant of the ZnO layers could be determined. Applying pressure to the multilayer structure while measuring I-V curves enables a study of the piezoelectric effect.

To analyze the optical properties of the ZnO layers, photoluminescence spectra could be measured, revealing information about the band gap and excitonic emissions.

Also, measurements of the superconducting properties of the YBCO layer underneath the ZnO should be conducted to determine whether there is zinc diffusion into the YBCO at levels too low to change the lattice. An analysis of the superconducting properties while changing the ZnO properties through the illumination with UV light might yield interesting results.

# Bibliography

- [1] M. D. Strikovsky, E. B. Klyuenkov, S. V. Gaponov, J. Schubert, and C. A. Copetti. Crossed fluxes technique for pulsed laser deposition of smooth YBaCuO films and multilayers. *Applied Physics Letters*, 63(8):1146–1148, 1993.
- [2] U. Ozgur, Ya. I. Alivov, C. Liu, A. Teke, M. A. Reshchikov, S. Dogan, V. Avrutin, S.-J. Cho, and H. Morkoc. A comprehensive review of ZnO materials and devices. *Journal of Applied Physics*, 98(4):041301, 2005.
- [3] Website Hokkaido University. [http://www.hokudai.ac.jp/science/science/H12\\_08/buturi/topics.html](http://www.hokudai.ac.jp/science/science/H12_08/buturi/topics.html), retrieved 05/01/2007.
- [4] Christopher Hammond. *The Basics of Crystallography and Diffraction*. Oxford University Press, 1997.
- [5] Douglas B. Chrisey and Graham K. Hubler, editors. *Pulsed Laser Deposition of thin films*. Wiley-Interscience, 1994.
- [6] René A. Haefler. *Oberflächen- und Dünnschicht-Technologie*. Springer-Verlag, 1987.
- [7] Marcus Menzel. Laserablation zur Herstellung von YBa<sub>2</sub>Cu<sub>3</sub>O<sub>7</sub>-Dünnschichten und anderen Oxiden. <http://www.pci.tu-bs.de/agbecker/laser.html>, retrieved 03/01/2007, retrieved 04/01/2007.
- [8] A. Klini, A. Manousaki, D. Anglos, and C. Fotakis. Growth of ZnO thin films by ultraviolet pulsed-laser ablation: Study of plume dynamics. *Journal of Applied Physics*, 98(12):123301, 2005.
- [9] Patzig. Herstellung und Untersuchung dünner Wismutschichten auf gitterunangepassten Substraten. Diploma thesis, Friedrich-Schiller-Universität Jena, 2006.
- [10] Rajiv K. Singh and D. Kumar. Pulsed laser deposition and characterization of high-T<sub>c</sub> YBaCuO superconducting thin films. *Materials Science and Engineering: R: Reports*, 22(4):113–185, April 1998.
- [11] J. C. S. Kools, T. S. Baller, S. T. De Zwart, and J. Dieleman. Gas flow dynamics in laser ablation deposition. *Journal of Applied Physics*, 71(9):4547–4556, 1992.
- [12] Rajiv K. Singh, D. Bhattacharya, and J. Narayan. Control of surface particle density in pulsed laser deposition of superconducting YBaCuO and diamondlike carbon thin films. *Applied Physics Letters*, 61(4):483–485, 1992.



- [13] B. Schey, W. Biegel, M. Kuhn, R. Klarmann, and B. Stritzker. Pulsed laser deposition of YBCO thin films on 7x20-cm substrates. *Applied Surface Science*, 127-129:540–543, May 1998.
- [14] Pierre Lorenz. Hochtemperatursupraleitende Josephsonkontakte auf großflächigen Substraten. Diploma thesis, Friedrich-Schiller-Universität Jena, 2005.
- [15] S. R. Foltyn, R. C. Dye, K. C. Ott, E. Peterson, K. M. Hubbard, W. Hutchinson, R. E. Muenchausen, R. C. Estler, and X. D. Wu. Target modification in the excimer laser deposition of YBCO thin films. *Applied Physics Letters*, 59(5):594–596, 1991.
- [16] Wolfgang Kautek, Bernhard Roas, and Ludwig Schultz. Formation of Y–Ba–Cu–oxide thin films by pulsed laser deposition: A comparative study in the UV, visible and IR range. *Thin Solid Films*, 191(2):317–334, October 1990.
- [17] Lars Ferchland. *Untersuchung zum Wachstum und zur Passivierung von dünnen Schichten aus Hochtemperatur-Supraleitern für die Anwendung bei Sensorbauelementen*. PhD thesis, Friedrich-Schiller-Universität Jena, 1999.
- [18] B. Holzapfel, B. Roas, L. Schultz, P. Bauer, and G. Saemann-Ischenko. Off-axis laser deposition of YBaCuO thin films. *Applied Physics Letters*, 61(26):3178–3180, 1992.
- [19] E. V. Pechen, A. V. Varlashkin, S. I. Krasnosvobodtsev, B. Brunner, and K. F. Renk. Pulsed-laser deposition of smooth high-Tc superconducting films using a synchronous velocity filter. *Applied Physics Letters*, 66(17):2292–2294, 1995.
- [20] C. Doughty, A.T. Findikoglu, and T. Venkatesan. Steady state pulsed laser deposition target scanning for improved plume stability and reduced particle density. *Applied Physics Letters*, 66(10):1276–1278, 1995.
- [21] Z. Trajanovic, S. Choopun, R. P. Sharma, and T. Venkatesan. Stoichiometry and thickness variation of YBaCuO in pulsed laser deposition with a shadow mask. *Applied Physics Letters*, 70(25):3461–3463, 1997.
- [22] Kazuya Kinoshita, Hiroshige Ishibashi, and Takeshi Kobayashi. Improved surface smoothness of YBaCuO films and related multilayers by ArF excimer laser deposition with shadow mask 'eclipse method'. *Japanese Journal of Applied Physics, Part 2: Letters*, 33(3B):L417–L420, March 1994.
- [23] Hanns-Ulrich Habermeier, Gunter Beddies, Bernd Leibold, Ganghua Lu, and Gunter Wagner. Y-Ba-Cu-O high temperature superconductor thin film preparation by pulsed laser deposition and RF sputtering: A comparative study. *Physica C: Superconductivity*, 180(1-4):17–25, September 1991.
- [24] J. Santiso, A. Moya, and F. Baudenbacher. Stoichiometry and surface morphology of YBaCuO thin films prepared by off-axis laser ablation. *SUPERCONDUCTOR SCIENCE & TECHNOLOGY*, 11(5):462–466, May 1998.

- [25] Soon-Gul Lee, Doo-Sup Hwang, Yong Ki Park, and Jong-Chul Park. Deposition angle-dependent morphology of laser deposited YBaCuO thin films. *Applied Physics Letters*, 65(6):764–766, 1994.
- [26] V. Boffa, T. Petrisor, L. Ciontea, U. Gambardella, and S. Barbanera. High-quality surface YBCO thin films prepared by off-axis pulsed laser deposition technique. *Physica C: Superconductivity*, 276(3-4):218–224, March 1997.
- [27] T. Schmauder, A. Waldauf, H. Wald, and P. Seidel. Influence of target-substrate angle on properties of laser deposited YBaCuO thin films and step-edge Josephson junctions. *Physica C: Superconductivity*, 333(1-2):23–30, May 2000.
- [28] T. Ohshima, R. K. Thareja, T. Ikegami, and K. Ebihara. Preparation of ZnO thin films on various substrates by pulsed laser deposition. *Surface and Coatings Technology*, 169-170:517–520, June 2003.
- [29] J. N. Leboeuf, K. R. Chen, J. M. Donato, D. B. Geohegan, C. L. Liu, A. A. Puretzky, and R. F. Wood. Modeling of dynamical processes in laser ablation. *Applied Surface Science*, 96-98:14–23, April 1996.
- [30] David B. Geohegan. Physics and diagnostics of laser ablation plume propagation for high-Tc superconductor film growth. *Thin Solid Films*, 220(1-2):138–145, November 1992.
- [31] Milton Ohring. *The Materials Science of Thin Films*. Academic Press, Inc. Harcourt Brace Jovanovich, 1992.
- [32] Semiconductor. Website Compound Semiconductor Lab. YSSSPRL, Institute of Physics and Applied Physics, Yonsei University. <http://ipap.yonsei.ac.kr/~fenian/semiconductor.htm>, retrieved 04/01/2007.
- [33] J. Mannhart, J. Bednorz, A. Catana, Ch. Gerber, and D. Schlom. *Materials and Crystallographic Aspects of HTc-Superconductivity*, chapter High-Tc thin films. Growth modes - structures - applications, pages 453–470. Kluwer Academic Pub, 1994.
- [34] C. C. Chang, X. D. Wu, R. Ramesh, X. X. Xi, T. S. Ravi, T. Venkatesan, D. M. Hwang, R. E. Muenchausen, S. Foltyn, and N. S. Nogar. Origin of surface roughness for c-axis oriented YBCO superconducting films. *Applied Physics Letters*, 57(17):1814–1816, 1990.
- [35] H. K. Onnes. On the sudden change in the rate at which the resistance of mercury disappears. *Comm. Leiden*, 124c, 1911.
- [36] Dirk Reimer. A Guide to Superconductivity. Website <http://www.physnet.uni-hamburg.de/home/vms/reimer/hhc/contents.html> retrieved 13/01/2007.

- [37] Paul Seidel. Supraleitung Grundlagen und Anwendung. Website Friedrich-Schiller-Universität. [http://www.physik.uni-jena.de/~tief/Lehre/SS2004/SL\\_03\\_charakteristische%20Eigenschaften%201\\_Seidel.pdf](http://www.physik.uni-jena.de/~tief/Lehre/SS2004/SL_03_charakteristische%20Eigenschaften%201_Seidel.pdf), retrieved 07/01/2007.
- [38] J. D. Jorgensen, B. W. Veal, A. P. Paulikas, L. J. Nowicki, G. W. Crabtree, H. Claus, and W. K. Kwok. Structural properties of oxygen-deficient YBCO. *Phys. Rev. B*, 41(4):1863, February 1990.
- [39] Werner Buckel and Reinhold Kleiner. *Supraleitung*. Wiley-VCH, 2004.
- [40] F. Beech, S. Miraglia, A. Santoro, and R. S. Roth. Neutron study of the crystal structure and vacancy distribution in the superconductor YBCO. *Phys. Rev. B*, 35(16):8778–8781, June 1987.
- [41] Peter Nagel, Volker Pasler, Christoph Meingast, Alexandre I. Rykov, and Setsuko Tajima. Anomalous Large Oxygen-Ordering Contribution to the Thermal Expansion of Untwinned YBCO Single Crystals: A Glasslike Transition near Room Temperature. *Phys. Rev. Lett.*, 85(11):2376–2379, September 2000.
- [42] K Kihara and G Donnay. Anharmonic thermal vibrations in ZnO. *Canadian Mineralogist*, 23:647–654, 1985.
- [43] Martin Beck. Untersuchungen zur Abscheidung von dünnen Zinkoxid-Schichten mittels Pulsed Laser Deposition. Diploma thesis, Friedrich-Schiller-Universität Jena, 2005.
- [44] Karsten J. Foos and Helmut Wipf. Sauerstoffdiffusion in YBCO. Website Institut für Festkörperphysik, TU Darmstadt, D-64289 Darmstadt. <http://www.fkp.physik.tu-darmstadt.de/Wipf/pages/ybco.htm> retrieved 04/01/2007, 1999.
- [45] Veit Grosse. Herstellung und Charakterisierung von epitaktischen Supraleiter-Isolator-Schichtsystemen. Diploma thesis, Friedrich-Schiller-Universität Jena, 2005.
- [46] Junichi Kawashima, Yasuji Yamada, and Izumi Hirabayashi. Critical thickness and effective thermal expansion coefficient of YBCO crystalline film. *Physica C: Superconductivity*, 306(1-2):114–118, September 1998.
- [47] D. C. Look, B. Claffin, Ya. I. Alivov, and S. J. Park. The future of ZnO light emitters. *physica status solidi (a)*, 201(10):2203–2212, 2004.
- [48] Yan Miao, Zhizhen Ye, Weizhong Xu, Fugang Chen, Xincui Zhou, Binghui Zhao, Liping Zhu, and Jianguo Lu. p-Type conduction in phosphorus-doped ZnO thin films by MOCVD and thermal activation of the dopant. *Applied Surface Science*, 252(22):7953–7956, September 2006.
- [49] David C Look. Electrical and optical properties of p-type ZnO. *Semiconductor Science and Technology*, 20(4):S55–S61, 2005.

- [50] Sang Hyuck Bae, Sang Yeol Lee, Beom Jun Jin, and Seongil Im. Pulsed laser deposition of ZnO thin films for applications of light emission. *Applied Surface Science*, 154-155:458–461, February 2000.
- [51] A. Fouchet, W. Prellier, B. Mercey, L. Mechin, V. N. Kulkarni, and T. Venkatesan. Investigation of laser-ablated ZnO thin films grown with Zn metal target: A structural study. *Journal of Applied Physics*, 96(6):3228–3233, 2004.
- [52] E. M. Kaidashev, M. Lorenz, H. von Wenckstern, A. Rahm, H.-C. Semmelhack, K.-H. Han, G. Benndorf, C. Bundesmann, H. Hochmuth, and M. Grundmann. High electron mobility of epitaxial ZnO thin films on c-plane sapphire grown by multistep pulsed-laser deposition. *Applied Physics Letters*, 82(22):3901–3903, 2003.
- [53] Sang Sub Kim and Byung-Teak Lee. Effects of oxygen pressure on the growth of pulsed laser deposited ZnO films on Si(0 0 1). *Thin Solid Films*, 446(2):307–312, January 2004.
- [54] A. Mitra, R. K. Thareja, V. Ganesan, A. Gupta, P. K. Sahoo, and V. N. Kulkarni. Synthesis and characterization of ZnO thin films for UV laser. *Applied Surface Science*, 174(3-4):232–239, April 2001.
- [55] S. V. Prasad, S. D. Walck, and J. S. Zabinski. Microstructural evolution in lubricious ZnO films grown by pulsed laser deposition. *Thin Solid Films*, 360(1-2):107–117, February 2000.
- [56] V. Savchuk, B. Kotlyarchuk, and M. Oszwaldowski. Production of Indium Doped Zinc Oxide Thin Films by Pulsed Laser Ablation. arXiv.org, cond-mat., 2005.
- [57] M. Zerdali, S. Hamzaoui, F.H. Teherani, and D. Rogers. Growth of ZnO thin film on SiO<sub>2</sub>/Si substrate by pulsed laser deposition and study of their physical properties. *Materials Letters*, 60(4):504–508, February 2006.
- [58] Frederik Claeysens, Andrew Cheesman, Simon J. Henley, and Michael N. R. Ashfold. Studies of the plume accompanying pulsed ultraviolet laser ablation of zinc oxide. *Journal of Applied Physics*, 92(11):6886–6894, 2002.
- [59] G. Götz. *High Energy Ion Beam Analysis of Solids*. Friedrich-Schiller-Universität Jena, Sektion Physik, 1986.
- [60] Sergei N. Maganov and Myong-hwan Hwanglo. *Surface analysis with STM and AFM: experimental and theoretical aspects of image analysis*. VHC, 1996.
- [61] Ray F. Egerton. *Physical principles of electron microscopy*. Springer, 2005.
- [62] J. A. BEARDEN. X-ray wavelengths. *Rev. Mod. Phys.*, 39(1):78–124, January 1967.

- [63] R.W. James. *The optical principles of the diffraction of x-rays*. Ox Bow Press, 1982.
- [64] Tobias Förster. Hochempfindliche Gradiometer für unabgeschirmte Messungen magnetischer Felder. Diploma thesis, Friedrich-Schiller-Universität Jena, 2006.
- [65] Paola Benzi, Elena Bottizzo, and Nicoletta Rizzi. Oxygen determination from cell dimensions in YBCO superconductors. *Journal of Crystal Growth*, 269(2-4):625–629, September 2004.
- [66] Ch. Kruger, K. Conder, H. Schwer, and E. Kaldis. The Dependence of the Lattice Parameters on Oxygen Content in Orthorhombic YBaCuO: A High Precision Reinvestigation of Near Equilibrium Samples. *Journal of Solid State Chemistry*, 134(2):356–361, December 1997.
- [67] S. Degoy, J. Jimenez, P. Martin, O. Martinez, A. C. Prieto, D. Chambonnet, C. Audry, C. Belouet, and J. Perriere. Oxygen content of YBaCuO thin films. *Physica C: Superconductivity*, 256(3-4):291–297, January 1996.
- [68] Jinhua Ye and Keikichi Nakamura. Quantitative structure analyses of YBaCuO thin films: Determination of oxygen content from x-ray-diffraction patterns. *Phys. Rev. B*, 48(10):7554–7564, September 1993.
- [69] C. B. Eom, J. Z. Sun, K. Yamamoto, A. F. Marshall, K. E. Luther, T. H. Geballe, and S. S. Laderman. In situ grown YBCO thin films from single-target magnetron sputtering. *Applied Physics Letters*, 55(6):595–597, 1989.
- [70] M. N. Iliev, P. X. Zhang, H. U. Habermeier, and M. Cardona. Raman spectroscopy as analytical tool for the local structure of YBaCuO thin films. *Journal of Alloys and Compounds*, 251(1-2):99–102, April 1997.
- [71] P. Richter, M. Kress, E. Mohler, H. G. Roskos, G. Jakob, and H. Adrian. Optical determination of the oxygen content of YBaCuO thin films by IR reflectance and transmittance measurements. *Physica C: Superconductivity*, 366(1):63–72, December 2001.
- [72] Crystallite Size Analysis 1 & 2. Website Department of Chemical Engineering and Materials Science, University of California, Davis. <http://www.matsci.ucdavis.edu/MatSciLT/EMS-162L/EMS-162L.htm>, retrieved 04/01/2007.
- [73] Sang-Moo Park, Tomoaki Ikegami, Kenji Ebihara, and Paik-Kyun Shin. Structure and properties of transparent conductive doped ZnO films by pulsed laser deposition. *Applied Surface Science*, 253(3):1522–1527, November 2006.
- [74] Rong-Ping Wang, Hachizo Muto, and Takeshi Kusumori. Growth of c-axis oriented GaN films on quartz by pulsed laser deposition. *Optical Materials*, 23(1-2):15–20, 2003.

- [75] F Licci and L Raffo. Interplay of electronic and structural features in Zn- and Fe-doped YBCO. *Superconductor Science and Technology*, 8(4):245–251, 1995.
- [76] Kouji Segawa and Yoichi Ando. Zn-doping effect on the normal-state charge transport in untwinned YBaCuO single crystals at low temperatures. *Physica C: Superconductivity*, 357-360(Part 1):30–33, September 2001.